CHAPTER 4

RESULTS AND DISCUSSION
MICROSTRUCTURAL, PHYSICAL AND MECHANICAL PROPERTIES

Binary and tertiary ceramic reinforced copper-based hybrid composites have been synthesized by liquid stir-casting technique as described in Chapter-3. Total eight hybrid composites have been developed by various ceramic reinforcements such as WC, Al_2O_3, ZrO_2, BN and B_4C including Cr particle based on the nominal composition. The developed binary reinforced copper-based composites have been designated as Cu-2Cr-1WC-1ZrO_2 (Hybrid composite-1 (HC-1)), Cu-2Cr-1WC-1Al_2O_3 (HC-2), Cu-2Cr-1WC-2ZrO_2 (HC-3) and Cu-2Cr-1WC-2Al_2O_3 (HC-4). Whereas, tertiary reinforced hybrid composites are designated as Cu-2Cr-1.5WC-1BN-0B_4C (HC-5), Cu-2Cr-1.5WC-1BN-0.5B_4C (HC-6), Cu-2Cr-1.5WC-1BN-1B_4C (HC-7), and Cu-2Cr-1.5WC-1BN-1.5B_4C (HC-8).

The detail SEM morphology and energy dispersive analysis of X-ray (EDAX) of reinforcing particles are reported in this chapter followed by the results organized according to the developed hybrid composite system. It is followed by the sequence of structural characterization by microstructural examination through EDAX, optical microscope, high resolution scanning electron microscope (HRSEM), XRD and mechanical properties like-hardness, compressive and tensile characteristics. The electrical conductivity and density of developed hybrid composites are also reported. The results have been discussed comprehensively on the basis of observations made during the characterizations.

4.1. Morphological study of reinforcing particles

Reinforcing phase need not essentially be in the long fibers form. It can be in the form of flakes, short fibers, particles, whiskers, sheets or continuous fibers. Therefore, in the current study the particles reinforcements are chosen to develop the metal matrix hybrid composites. The reinforcing particles are analyzed using the SEM equipped with EDAX instruments and their results are displayed in the Figs. 4.1 to 4.3. Figures 4.1 (a) to 4.1 (f) show the morphology of the WC, Cr, B_4C, Al_2O_3, BN and ZrO_2 particles respectively. The particles morphology usually plays an important role to influence the materials properties. Figure 4.1 (a) exhibits the homogeneous, spherical and non-agglomerated particles morphology of WC. Irregular, bulky and fractured stone like morphology of Cr is observed, as revealed in Fig. 4.1 (b). Figure 4.1 (c) displays the sharp edged and quite agglomerated morphology of the B_4C particles. Plate like and non-agglomerated morphology of Al_2O_3 particles are depicted in Fig. 4.1 (d). However, Fig. 4.1 (e) shows the flaky, regular and very thin morphology of BN particles. The homogeneous, quite spherical, shiny and agglomerated morphology of the ZrO_2 is observed, as depicted in Fig. 4.1 (f).

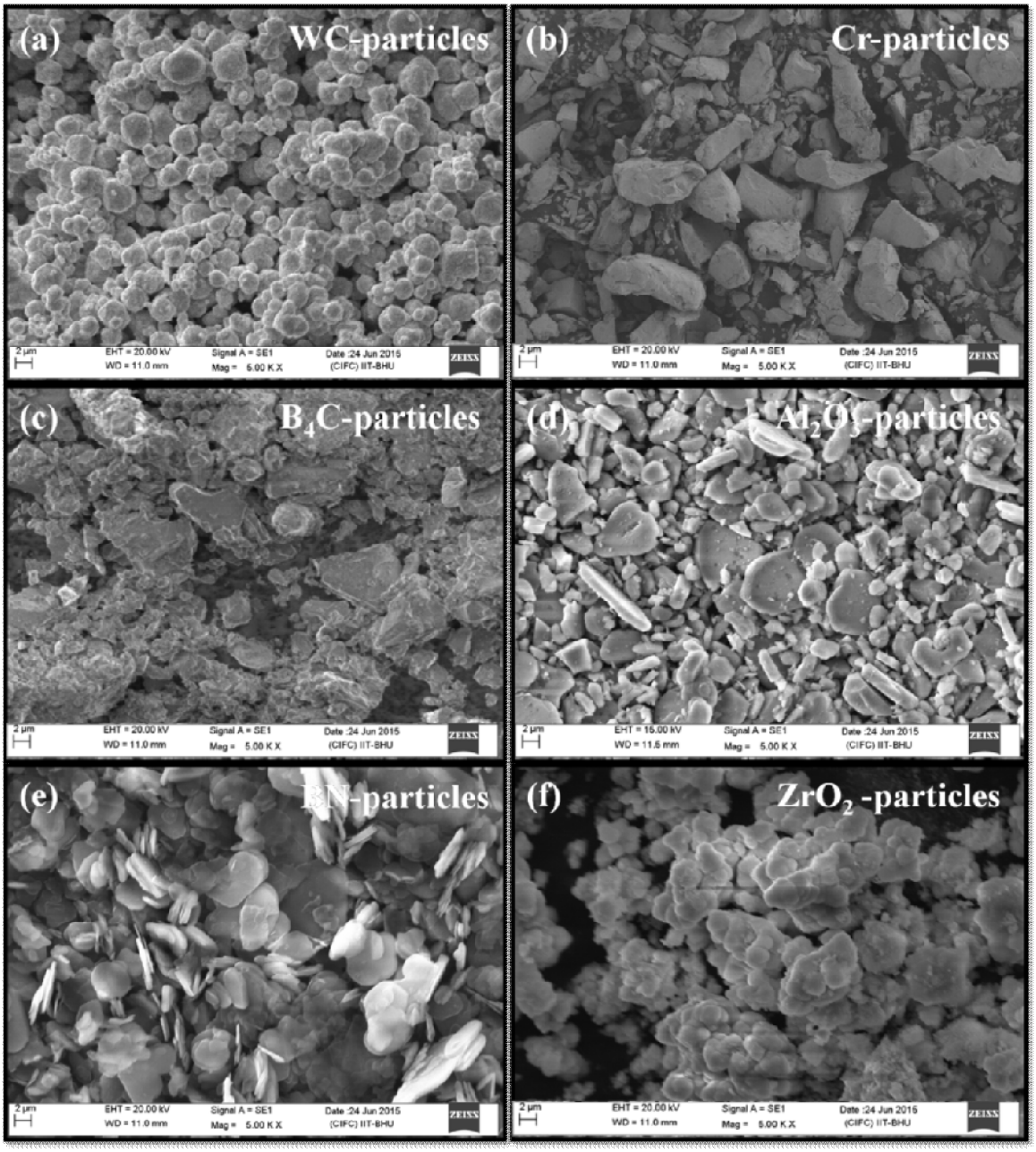

Fig.4.1. SEM morphology of (a) WC-particles, (b) Cr-particles, (c) B_4C-particles, (d) Al_2O_3-particles, (e) BN-particles and (f) ZrO_2-particles

Figures 4.2 (a) to (f) display the particles size distribution of the reinforcing particles. Figure 4.2 (a) shows the particle size distribution of WC that is in the range of 1.5 - 2.5 μm. Particle size of Cr lies in the range of 50 - 70 μm as depicted in Fig. 4.2 (b). However, the particle size distribution of B_4C lies in the range of 30 - 50 μm as depicted in Fig. 4.2 (c).

Figure 4.2 (d) to (f) exhibit the particle size distribution of Al_2O_3, BN and ZrO_2 which is lying in the range of 1.0 - 2.0, 4.0 - 4.5 and 1.5 - 2.0 μm respectively. The particle size of reinforcement is one of the major parameter to observe the changes in properties of any materials. The appropriate size of reinforcing particle to incorporate in the metal matrix should be lie in the range of 1.0 - 50.0 μm (Chawla, 2012), hence, all the reinforcing particles are selected in that appropriate size range.

Figure 4.3 (a) to (f) exhibit the EDAX spectrum of WC, Cr, B_4C, Al_2O_3, BN and ZrO_2 reinforcing particles, respectively. This investigation is basically done to observe the presence and purity of element in the respective reinforcing particles. Figure 4.3 (a) displays the intensity peak of W and C only no other peaks found, their weight and atomic percentage are reported in the adjacent table. However, Fig. 4.3 (b) shows the intensity peak of carbon as impurity in the EDAX spectrum of Cr, their weight and atomic percentage are given in the table adjacent to its spectrum. The intensity peak of carbon may be due to the carbon tape used to mount the sample for EDAX characterizations. The additional intensity peak is not observed apart from their respective element intensity peak in the EDAX spectrum of all the B_4C, Al_2O_3, BN and ZrO_2. The tables adjacent to their respective EDAX spectrum display the details of their weight and atomic percentage of the respective elements present in the spectrum. Therefore, this investigation of the reinforcing particles suggests that it does not contain any kind of impure materials.

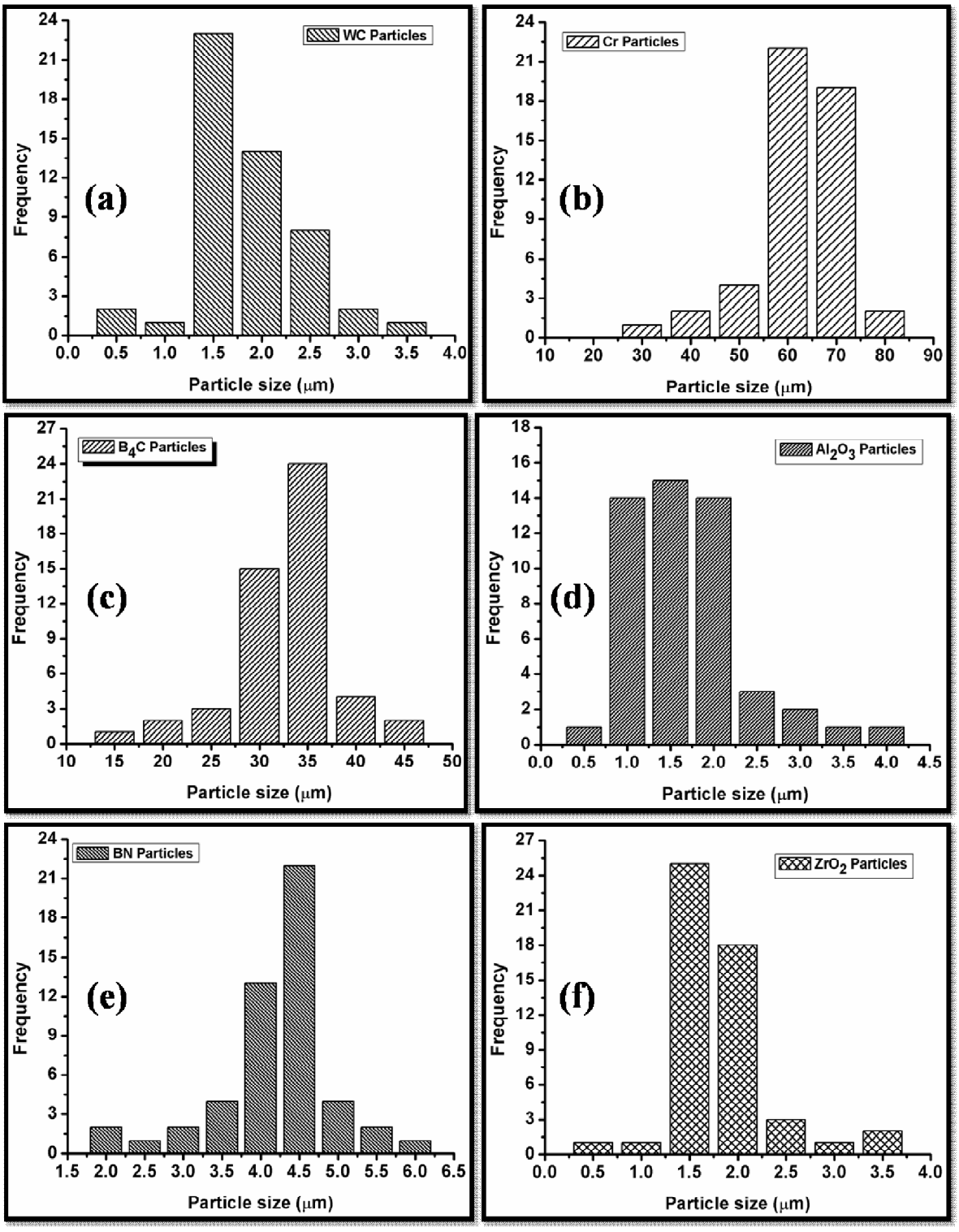

Fig.4.2. Particle size distribution of (a) WC-particles, (b) Cr-particles, (c) B_4C-particles, (d) Al_2O_3-particles, (e) BN-particles and (f) ZrO_2-particles

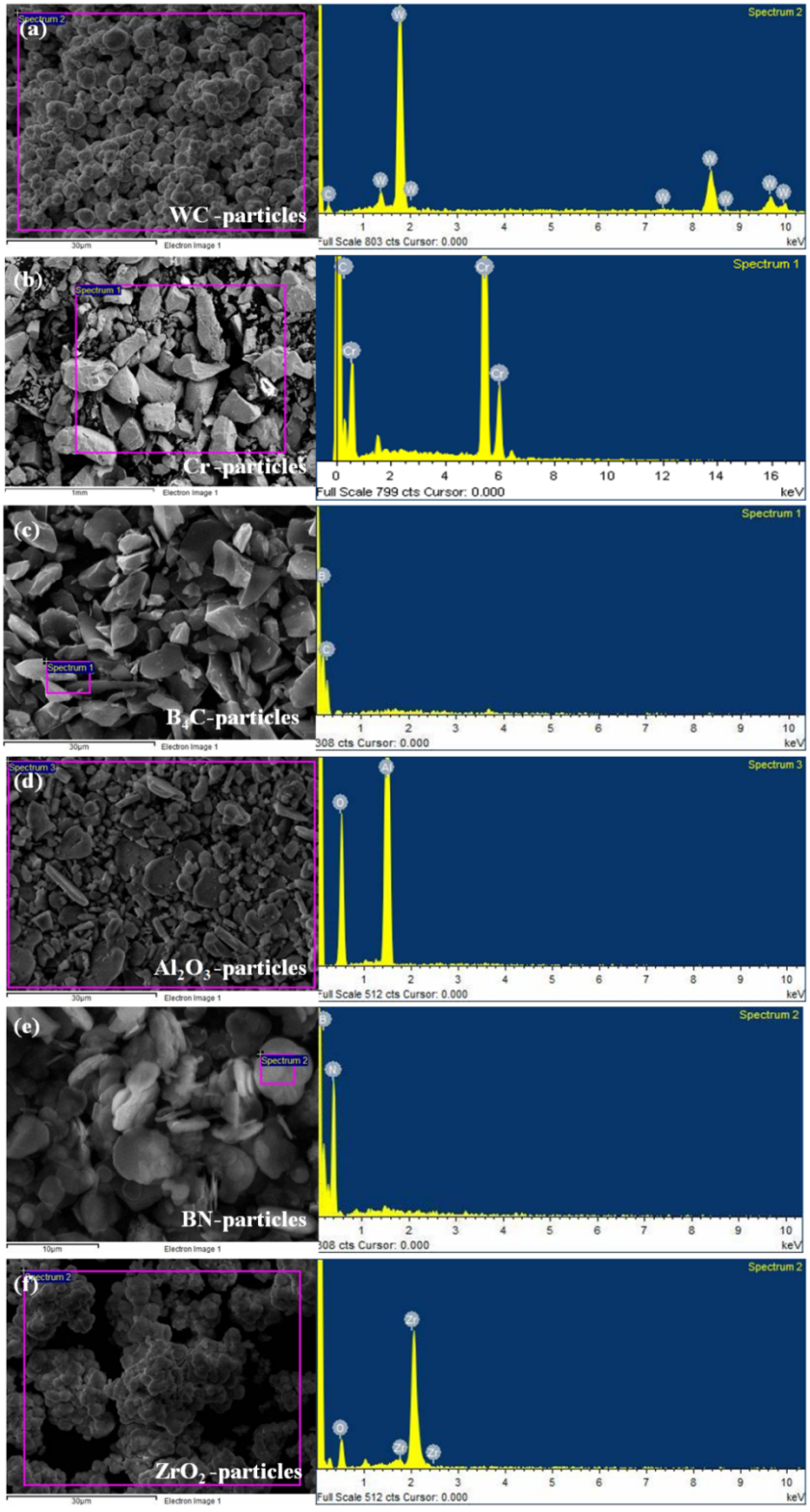

Element	Weight%	Atomic%
C K	24.63	83.34
W M	75.37	16.66
Totals	100.00	

Element	Weight%	Atomic%
C K	21.05	53.58
Cr K	78.95	46.42
Totals	100.00	

Element	Weight%	Atomic%
B K	45.04	47.66
C K	54.96	52.34
Totals	100.00	

Element	Weight%	Atomic%
O K	50.09	62.86
Al K	49.91	37.14
Totals	100.00	

Element	Weight%	Atomic%
B K	17.36	21.39
N K	82.64	78.61
Totals	100.00	

Element	Weight%	Atomic%
O K	31.20	72.11
Zr L	68.80	27.89
Totals	100.00	

Fig.4.3. EDAX spectrum of (a) WC-particles, (b) Cr-particles, (c) B_4C-particles, (d) Al_2O_3-particles, (e) BN-particles and (f) ZrO_2-particles

4.2. Binary reinforced copper-based hybrid composites

4.2.1. Microstructural study

Figures 4.4 (a) to (e) show the EDAX spectrum of the CC and binary reinforced hybrid composites i.e. HC-1, HC-2, HC-3 and HC-4, respectively. The hybrid composites show the intensity peaks of respective reinforcing materials with their weight and atomic percentage in the table which clearly indicated by EDAX spectrums. However, the EDAX spectrum of the CC shows the unwanted intensity peak of oxygen apart from intensity peak of copper. The unwanted intensity peak of silicon is also observed in the EDAX spectrum of HC-2 and HC-4.

Figures 4.5 (a) to (c) display the HR-SEM micrograph of the CC, HC-3, and HC-4 respectively. Figure 4.5 (a) shows the micrograph of CC in which the evidence of any kind of foreign element is absent and only smooth surface of copper can be observed. However, Fig. 4.5 (b) and (c) show very nicely the presence of reinforcing particles and its homogeneous distribution in the copper matrix. The micrograph of the hybrid composites reveals that the reinforcing phases are entrapped in the metal matrix by mechanical bonding. Reinforcing particles such WC, ZrO_2 and Al_2O_3 can be seen in the micrograph of HC-3 and HC-4 as revealed in Fig. 4.5 (b) and (c). Fig. 4.5 (b') and (c') display the enlarged view of the corresponding inset areas in Fig. 4.5 (a) and (b).

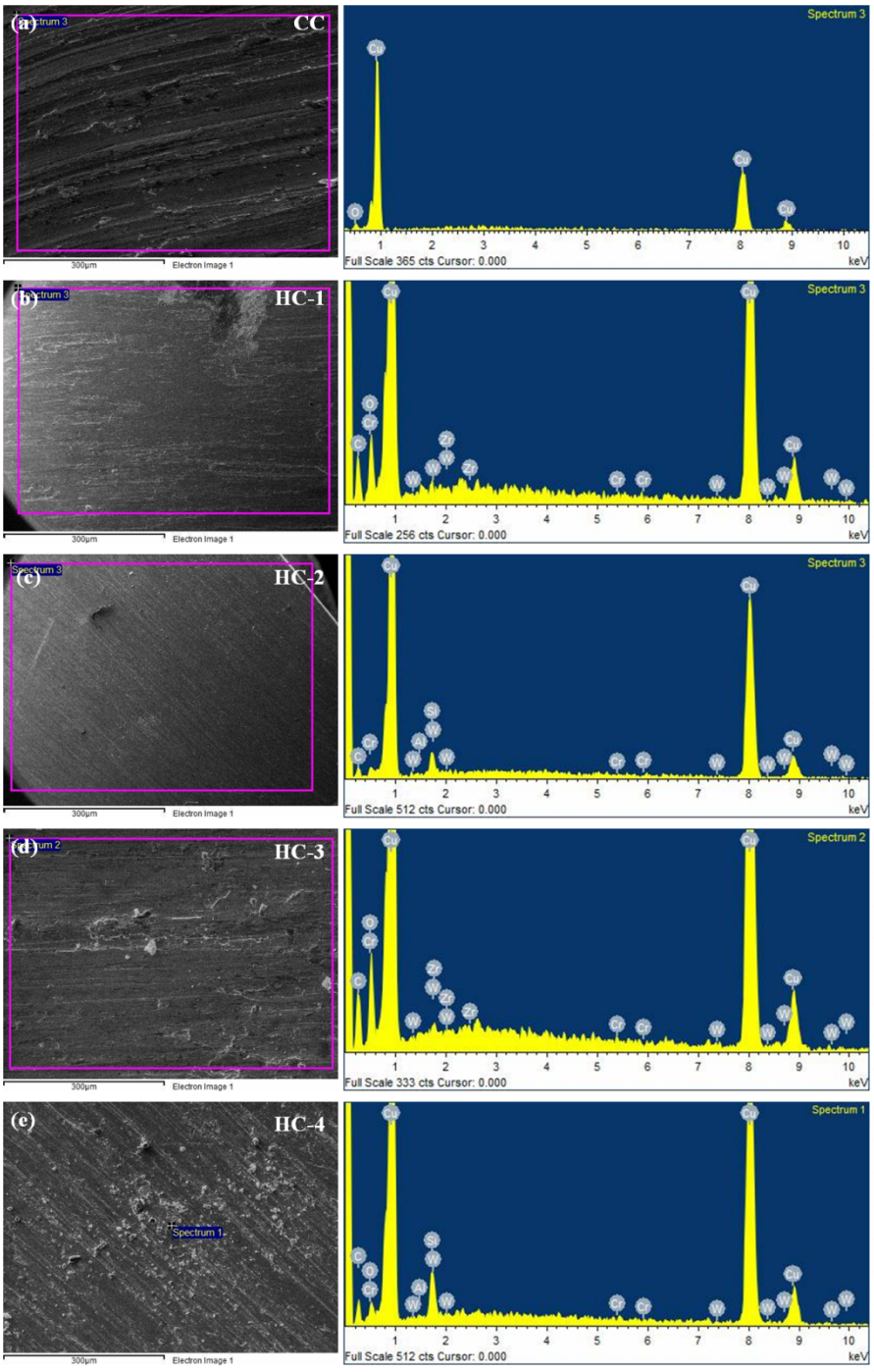

Element	Weight%	Atomic%
O K	4.26	15.03
Cu K	95.74	84.97
Totals	100.00	

Element	Weight%	Atomic%
C K	26.91	59.59
O K	8.20	13.51
Cr K	0.20	0.35
Cu K	64.58	26.45
Zr L	0.10	0.10
W M	0.28	0.04
Totals	100.00	

Element	Weight%	Atomic%
C K	23.12	60.48
Al K	0.02	0.02
Si K	0.99	1.97
Cr K	0.14	0.08
Cu K	75.73	37.44
W M	0.92	0.16
Totals	100.00	

Element	Weight%	Atomic%
C K	17.96	46.97
O K	8.68	17.03
Cr K	0.09	0.06
Cu K	72.28	35.72
Zr L	0.32	0.11
W M	0.67	0.11
Totals	100.00	

Element	Weight%	Atomic%
C K	15.55	46.13
O K	2.54	5.65
Al K	0.28	0.37
Si K	2.67	3.56
Cr K	0.21	0.14
Cu K	78.75	44.15
W M	0.16	0.03
Totals	100.00	

Fig.4.4. The EDAX spectrum of (a) CC, (b) HC-1, (c) HC-2, (d) HC-3, and (e) HC-4

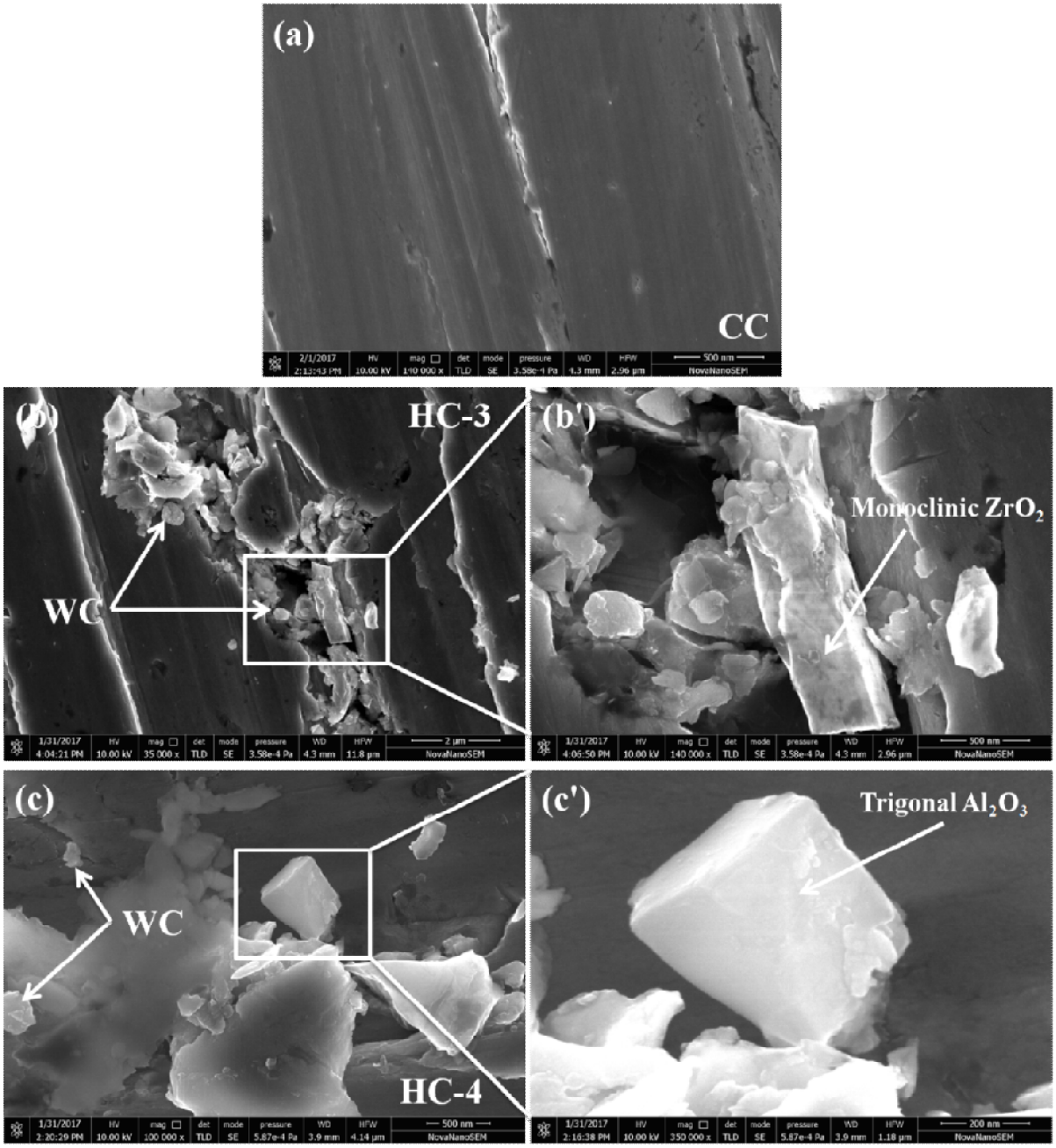

Fig.4.5. HR-SEM micrograph of (a) CC, (b) HC-3 and (c) HC-4

Figures 4.6 (a) to (e) show the HR-SEM morphology of CC, HC-1, HC-2, HC-3 and HC-4 with selected area for corresponding color dot mapping, depicted in Figs. 4.6 (a') to (e') and respective EDAX spectrum as depicted in Figs. 4.6 (a'') to (e''). This investigation is accomplished to make sure that the developed hybrid composites contain the reinforcing

particles. Figure 4.6 (a') shows the color dot mapping of the selected area in HR-SEM micrograph of CC that does not display the color dots apart from the O and Cu. However, Color dot mapping of respective hybrid materials shows the significant presence of different reinforcing elements and its matrix, which are designated with different color coding. The color coding of each elements with their percentage are highlighted on the top right corner of the respective dot mappings, as depicted in Figs. 4.6 (b') to (e'). However, corresponding EDAX spectrum of the materials reveals the significant presence of the reinforcing elements with their weight and atomic percentage, as depicted in Figs. 4.6 (b") to (e"). From the EDAX spectrum as depicted in Figs 4.6 (b") to (e"), it is observed that the weight and atomic percentage of Zr and Al elements increases as the reinforcing percentage of ZrO_2 and Al_2O_3 in copper increases from 1 to 2 wt%.

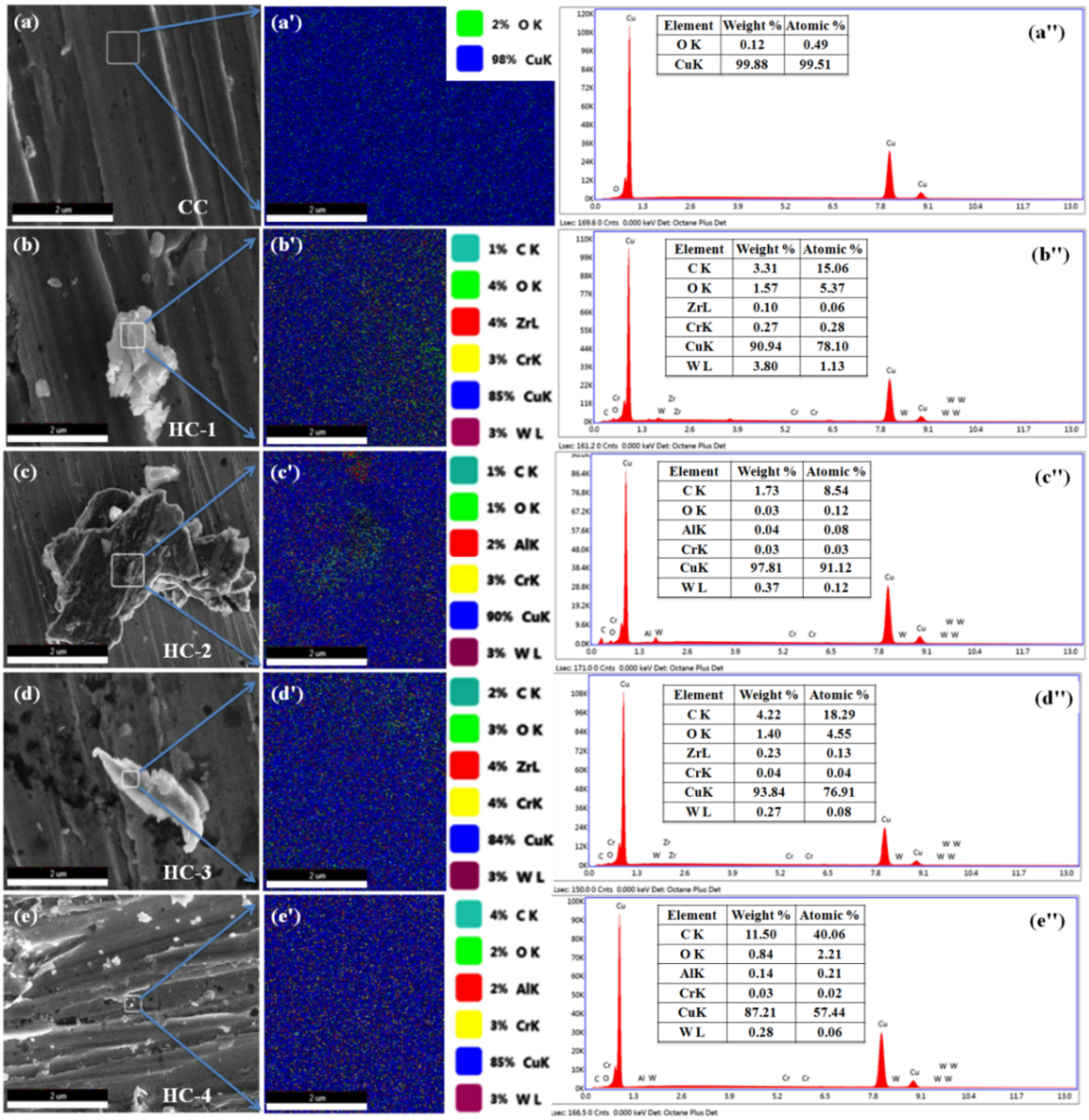

Fig.4.6. HR-SEM morphology of (a) CC, (b) HC-1, (c) HC-2, (d) HC-3, (e) HC-4, corresponding color dot mapping with color coding (a')–(e') and respective EDAX spectrum with report (a")–(e")

The X-Ray Diffraction (XRD) analysis of CC, HC-1, HC-2, HC-3 and HC-4 with variable weight percentage of Al_2O_3 and ZrO_2 has been carried out. The XRD spectrum of the CC and copper-based hybrid composites are depicted in Fig. 4.7, and the results have been compared with JCPDS data. From the Fig. 4.7, it is observed that the ceramic reinforced copper-based hybrid composites contain all the original peaks of copper only, no others

peaks are found in the diffraction pattern. However, the Bragg peak intensity and peak broadening are found different from CC that is attributed to the reinforcement of ceramic particles to the copper matrix. The full width at half maxima (FWHM) of XRD Bragg peak of the materials is evaluated by curve fitting and reported in the Table 4.1. From the Table 4.1, it is observed the FWHM of XRD Bragg peak in hybrid composites is higher compared with CC.

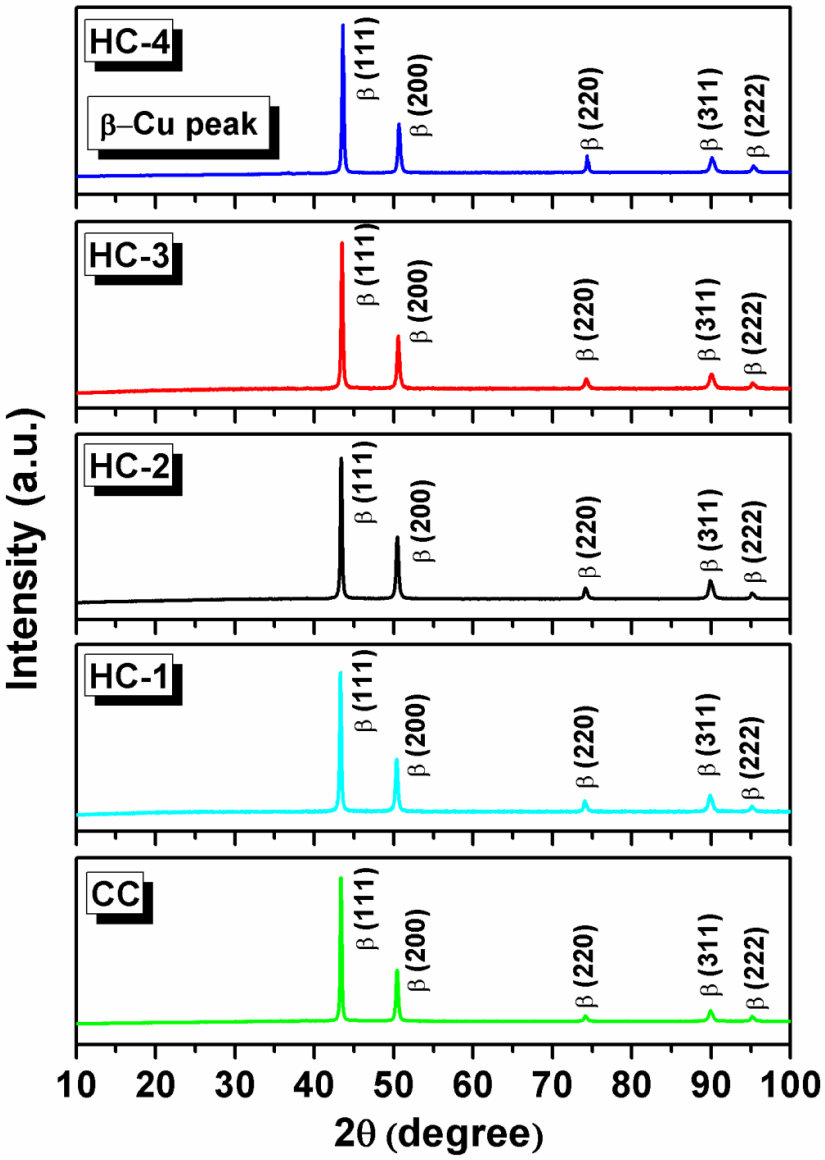

Fig.4.7. XRD pattern of the CC and binary reinforced hybrid composites

Table 4.1. Details of FWHM (β) of the cast copper and binary reinforced hybrid composites with their respective peak positions and diffraction planes

Peak position (2-deg.)	Diffraction planes	FWHM (β-deg.) of CC	FWHM (β-deg.) of HC-1	FWHM (β-deg.) of HC-2	FWHM (β-deg.) of HC-3	FWHM (β-deg.) of HC-4
43.080	(111)	0.2302	0.2492	0.2540	0.2565	0.2720
50.457	(200)	0.3373	0.3537	0.3610	0.3643	0.3577
74.184	(220)	0.4632	0.4558	0.4814	0.5039	0.4204
89.949	(311)	0.5965	0.6140	0.6146	0.6697	0.7247
95.205	(222)	0.5780	0.5877	0.6446	0.6730	0.8522

4.2.2. Physical properties

Table 4.2 shows the detail variation of the experimental density, theoretical density, relative density, porosity and electrical conductivity of CC, HC-1, HC-2, HC-3 and HC-4. It is observed that the experimental density of the hybrid composites is lower compared with CC. However, the variation of experimental density among hybrid composites is also observed. The experimental density of Al_2O_3 reinforced i.e. HC-2 and HC-4 is higher than ZrO_2 reinforced i.e. HC-1 and HC-3. HC-4 displays the highest density among all hybrid composites. From the Table 4.2, it is observed that the experimental density of ZrO_2 reinforced hybrid composites decreases with increase content of ZrO_2 in copper matrix. However, experimental density of Al_2O_3 reinforced hybrid composites increases with increasing content of Al_2O_3.

From the Table 4.2, it is also observed that the theoretical density of the hybrid composites is observed lower as compared with its matrix. The theoretical density of the hybrid composites materials shows a decreasing tendency on the increasing content of reinforcements. However, the relative density and porosity of the hybrid composites are found fluctuating in nature. Although, the relative density and porosity of the hybrid composites are lower compared with CC. among the hybrid composites, alumina reinforced hybrid composites (HC-2 and HC-4) display low porosity and higher relative density as compared with zirconia reinforced hybrid composites (HC-1 and HC-3). It is also clear that the porosity of the hybrid composites increases with increasing zirconia content however it decreases with increasing alumina content as depicted in Table 4.2.

Table 4.2 displays the behavior of electrical conductivity of CC, HC-1, HC-2, HC-3 and HC-4. The electrical conductivity of the developed materials are reported in percentage of international annealed copper standard (%IACS). Table 4.2 shows the electrical conductivity of CC, HC-1, HC-2, HC-3 and HC-4 is 82, 25, 39, 20 and 55 %IACS respectively. Hybrid composites display the lower electrical conductivity as compared with CC. The variation in electrical conductivity is also observed with variable content of ceramic reinforcements, as the percentage of ZrO_2 increases from 0 to 2 wt% with constant wt% of WC and Cr, the conductivity decreases from 82 to 20 %IACS. However, with increasing content of the Al_2O_3 from 0 to 2 wt% with the same wt% of WC and Cr, the conductivity decreases from 82 to 55 %IACS. Overall, both hybrid composites display low electrical conductivity as compared to CC. However, the Al_2O_3 based hybrid composite shows a better conductivity compared with ZrO_2 reinforced.

Table 4.2. Variation of experimental density, theoretical density, relative density, porosity and electrical conductivity of CC, HC-1, HC-2, HC-3 and HC-4

Materials	Experimental density (ED) ($g.cm^{-3}$)	Theoretical density (TD) ($g.cm^{-3}$)	Relative density (RD) (%)	Porosity (%)	%IACS
CC	8.33± 0.25	8.96	92.97± 0.25	~7	82±5
HC-1	7.55± 0.2	8.95	84.36± 0.2	~15	25±2
HC-2	7.67± 0.15	8.94	85.80± 0.15	~14	39±3
HC-3	7.45± 0.3	8.92	83.52± 0.3	~16	20±2
HC-4	7.88± 0.25	8.89	88.64± 0.25	~11	55±4

4.2.3. Mechanical properties

Figure 4.8 (a) shows the behaviour of Brinell hardness of CC, HC-1, HC-2, HC-3 and HC-4. Hardness influences the performance of copper-based metal matrix hybrid composites in its applications. The copper hybrid composites exhibit the higher Brinell hardness as compared with CC as shown in Fig. 4.8 (a). It is also observed that there is increase in the hardness with increasing content of the Al_2O_3 and ZrO_2 wt%, which reveals the good stability of reinforcing particles in copper matrix. An improvement of 15.58, 27.79, 35.06, and 44.93% in Brinell hardness of HC-1, HC-2, HC-3, and HC-4 is observed compared with CC, respectively.

The behaviour of compressive strength of CC, HC-1, HC-2, HC-3 and HC-4 is depicted in Fig. 4.8 (b). From the Fig. 4.8 (b), it is observed that the compression strength of the developed hybrid composites is higher as compared with CC. The significant increase in compressive strength of Al_2O_3 reinforced copper hybrid composites observed compared with

CC and ZrO_2 reinforced hybrid composite Overall, Al_2O_3 reinforced hybrid composites have better compressive strength compared with others. An improvement of 15.16, 24.48, 35.27, and 47.8% in compressive strength compared with CC is observed in HC-1, HC-2, HC-3, and HC-4 respectively.

The variation of ultimate tensile strength (UTS) of CC, HC-1, HC-2, HC-3 and HC-4 are depicted in Fig. 4.8 (c). Figure 4.8 (c) exhibits the UTS of the hybrid composites are comparatively higher than that of CC. An improvement of 20.53, 49.55, 54.01, and 71.87% in UTS is observed in HC-1, HC-2, HC-3, and HC-4 respectively compared with CC. It is observed that the UTS of hybrid composites increase as the content of ceramic reinforcement increases as depicted in Fig. 4.8 (c). HC-4 exhibits the highest UTS value among all the materials developed.

Figures 4.9 (a) to (e) shows the SEM micrograph of the fractured surface of the CC, HC-1, HC-2, HC-3 and HC-4, respectively. The hybrid composites display a different fractured morphology compared with CC. The presence of the pores and larger dimples are observed in the micrograph of CC as depicted in Fig. 4.9 (a). However, the presence of smaller dimples is observed in the entire fracture surface morphology of hybrid composites, compared with CC morphology. The reinforcing particles are also observed in the micrograph of fractured surface that are revealed by the arrow in the entire micrograph of hybrid composites as shown in Figs. 4.9 (b) to (e).

Figures 4.10 (a) to (e) show the EDAX spectrum of the fractured surface of CC, HC-1, HC-2, HC-3, and HC-4, respectively. Figure 4.10 (a) shows the EDAX spectrum of fractured surface of CC which displays the intensity peak of oxygen and copper only with their weight and atomic percentage. The EDAX spectrum of HC-1 as revealed in Fig. 4.10

(b) exhibits the absence of Zr intensity peak, however rest elemental intensity peaks are observed with their weight and atomic percentage. The similar case is observed in the EDAX spectrum of HC-2 where, the Al intensity peak is not found, however the rest of elemental intensity peaks are observed. The EDAX spectrum of HC-3 and HC-4 reveal the intensity peak of all the reinforcing elements with their weight and atomic percentage without any additional elemental intensity peaks as shown in Figs. 4.10 (d) and (e).

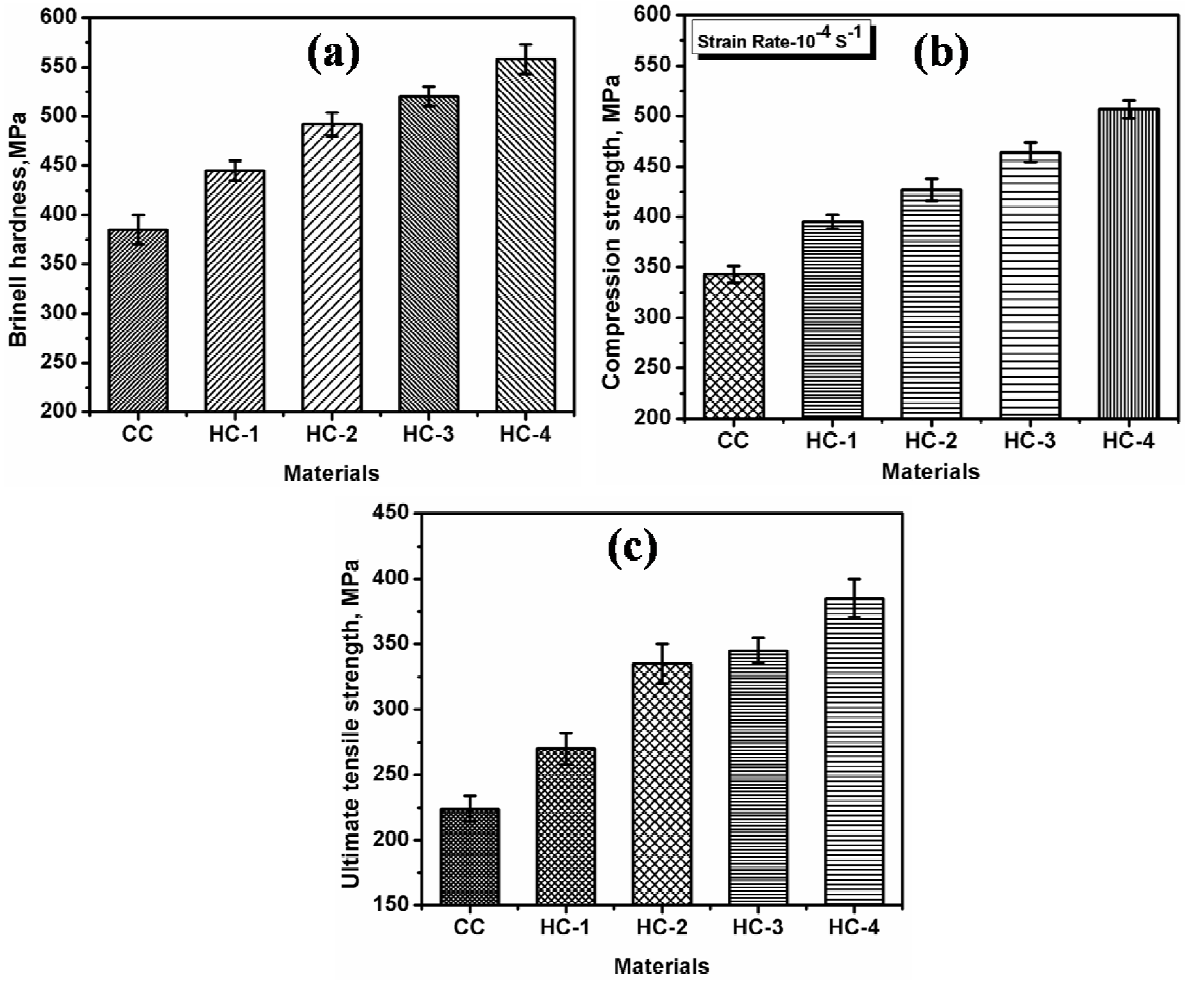

Fig.4.8. The variation of properties of binary reinforced hybrid composites (a) Brinell hardness, (b) Compression strength, (c) Ultimate tensile strength

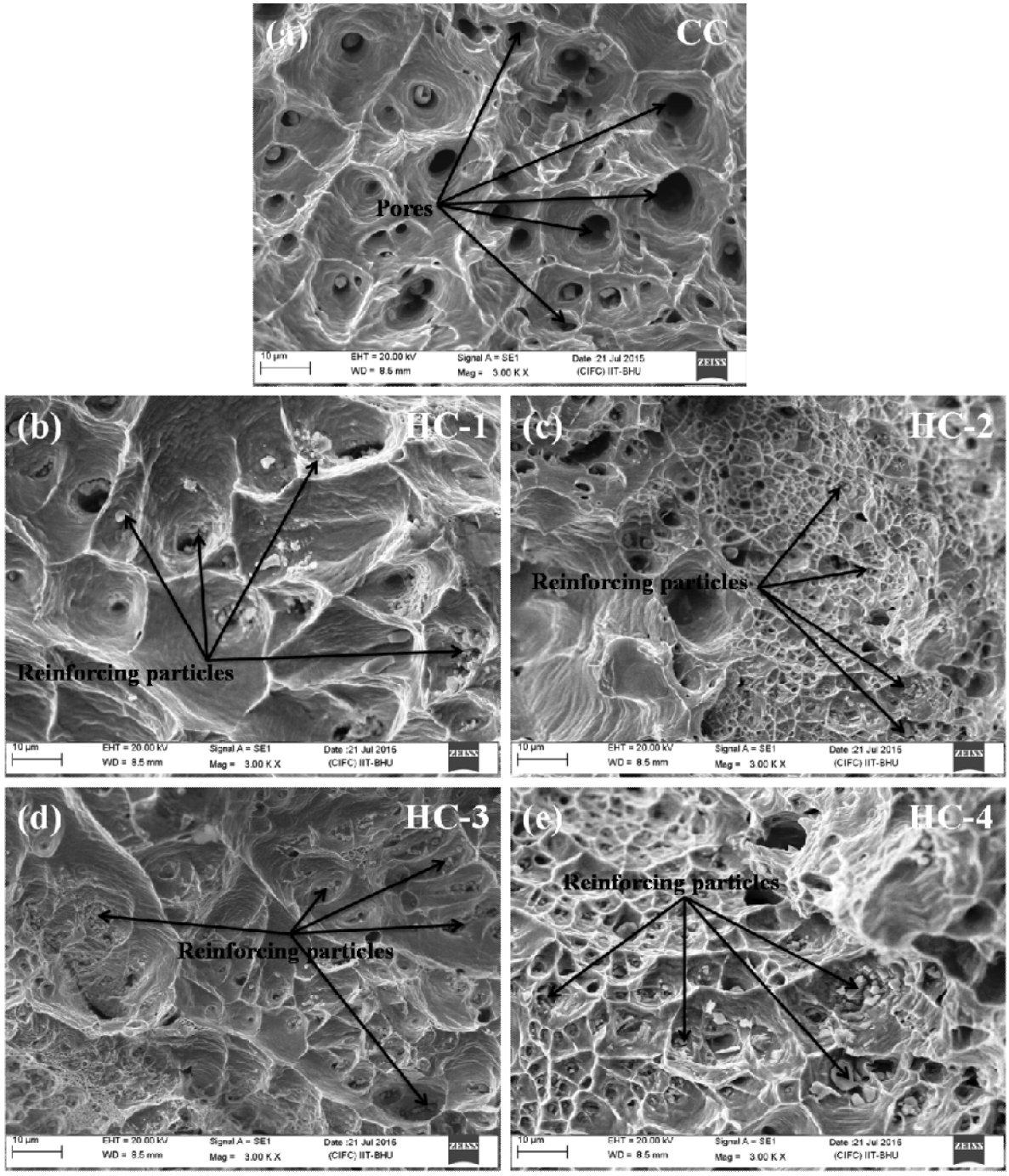

Fig.4.9. The SEM micrograph of fractured surface of (a) CC, (b) HC-1, (c) HC-2, (d) HC-3, and (e) HC-4

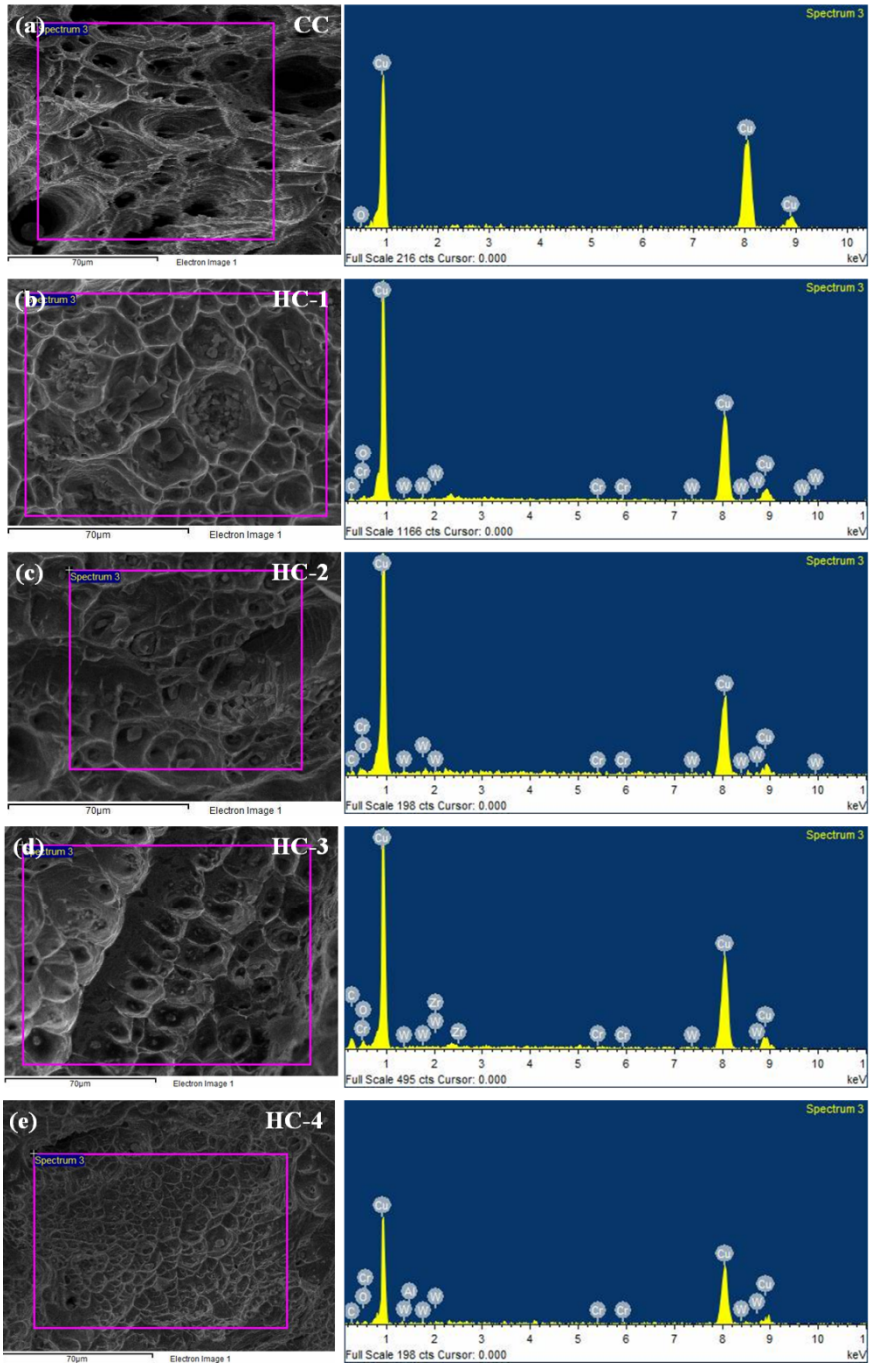

Element	Weight%	Atomic%
O K	0.23	0.90
Cu K	99.77	99.10
Totals	100.00	

Element	Weight%	Atomic%
C K	10.09	30.64
O K	2.18	4.70
Cr K	0.29	0.16
Cu K	86.31	64.27
W M	1.13	0.23
Totals	100.00	

Element	Weight%	Atomic%
C K	11.69	36.46
O K	2.10	4.97
Cr K	0.51	0.37
Cu K	82.56	57.55
W M	3.14	0.65
Totals	100.00	

Element	Weight%	Atomic%
C K	8.46	16.69
O K	3.20	9.79
Cr K	0.28	0.28
Cu K	84.37	70.86
Zr L	1.58	1.35
W M	2.11	1.03
Totals	100.00	

Element	Weight%	Atomic%
C K	13.92	40.67
O K	4.44	12.61
Al K	1.32	1.34
Cr K	0.20	0.11
Cu K	78.03	44.25
W M	2.09	1.02
Totals	100.00	

Fig.4.10. The EDAX spectrum of fractured surface of (a) CC, (b) HC-1, (c) HC-2, (d) HC-3 and (e) HC-4

4.3. Tertiary reinforced copper-based hybrid composites

4.3.1. Microstructural study

Figures 4.11 (a) to (e) show the EDAX spectrum of the CC and tertiary reinforced hybrid composites i.e. HC-5, HC-6, HC-7, and HC-8, respectively. EDAX employ the X-ray spectrum emitted by a solid specimen bombarded with a concentrated beam of electron to achieve a localized chemical analysis. EDAX spectrum of hybrid composites reveals the presence of all the reinforcing elements in the developed copper hybrid composites shown by their respective intensity of peak, weight, and atomic percentage. However, from the Fig. 4.11, it is observed that the intensity peak of boron element is absent in the entire EDAX spectrum of the developed hybrid composites. The intensity peak of the oxygen is observed in the entire EDAX spectrum as shown in Figs. 4.11 (a) to (e).

Figures 4.12 (a) to (e) show the typical microstructure of the CC, HC-5, HC-6, HC-7, and HC-8, respectively at 100× magnification. The changes in the microstructure of hybrid composites can be easily observed compared with CC microstructures, which means the reinforcement of the ceramic particles have played a significant role in the copper matrix. It is also observed that the grain refinement takes place in microstructure of HC-5, HC-6, and HC-7 as shown in Fig. 4.12 (b) to (d) respectively. The microstructure of the CC shows twins and these twins (Σ3) grain boundaries contain various facets with different crystallography that is clearly depicted in Fig. 4.12 (a) and Fig 4.13. It may be possible in other copper-based hybrid materials also.

The microstructure of CC and sections of Σ3 CSL (coincidence site lattice) at right angles to the {110} gradient axis with arrangement of different facets and micrograph of intersections of $(100)_{CSL}$ with other facets are depicted in Fig 4.13.

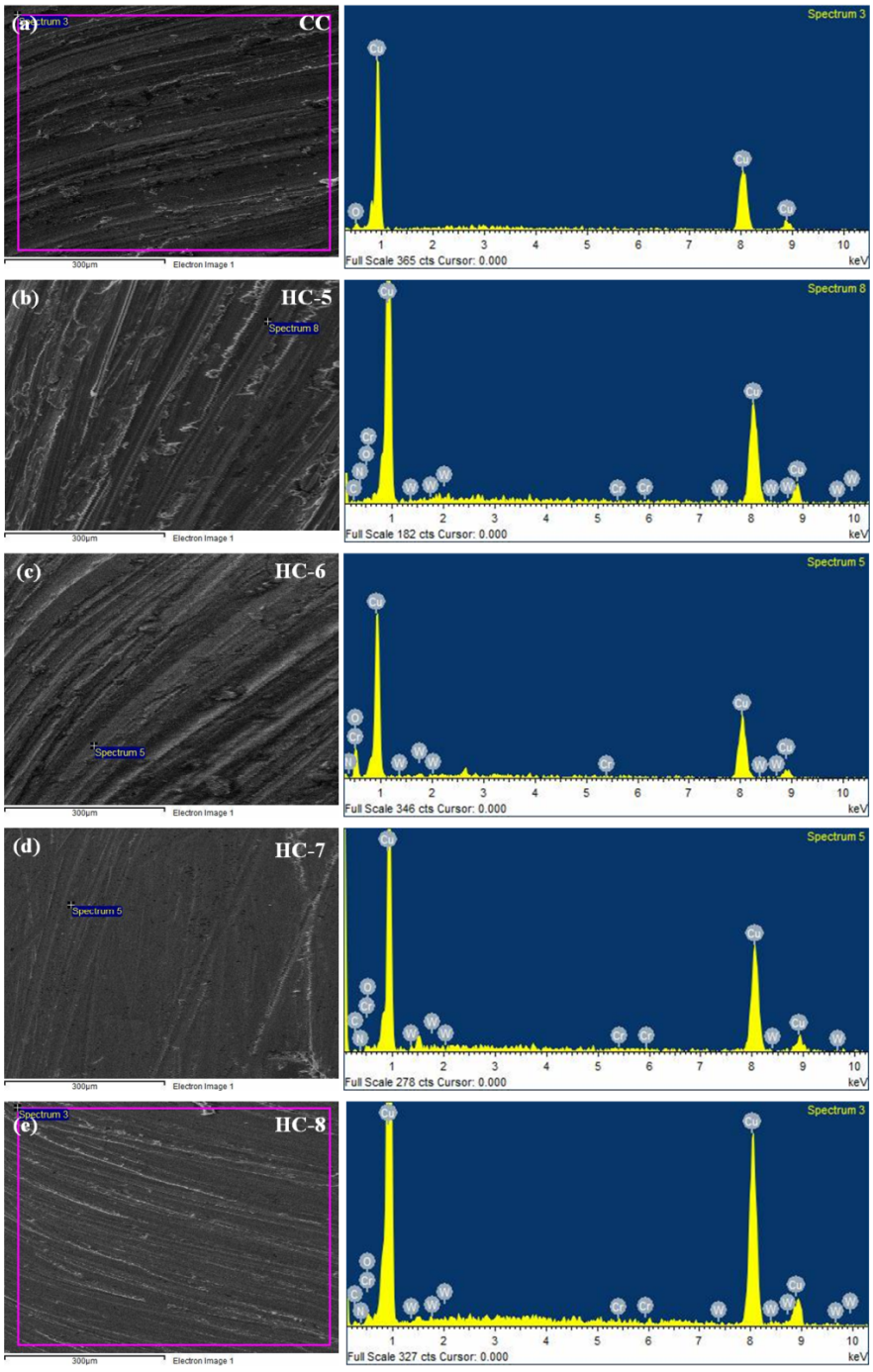

Element	Weight%	Atomic%
O K	4.26	15.03
Cu K	95.74	84.97
Totals	100.00	

Element	Weight%	Atomic%
C K	13.45	39.75
N K	3.40	8.61
O K	3.12	6.93
Cr K	0.04	0.03
Cu K	79.96	44.68
W M	0.03	0.01
Totals	100.00	

Element	Weight%	Atomic%
C K	22.21	46.49
N K	2.11	3.79
O K	17.13	26.92
Cr K	0.29	0.14
Cu K	56.73	22.45
W M	1.53	0.21
Totals	100.00	

Element	Weight%	Atomic%
C K	11.82	38.39
N K	1.82	5.06
O K	2.19	5.34
Cr K	0.04	0.03
Cu K	82.94	50.93
W M	1.20	0.25
Totals	100.00	

Element	Weight%	Atomic%
C K	11.51	37.68
N K	1.20	3.36
O K	2.76	6.79
Cr K	0.04	0.03
Cu K	84.08	52.04
W M	0.41	0.09
Totals	100.00	

Fig.4.11. EDAX Spectrum of (a) CC, (b) HC-5, (c) HC-6, (d) HC-7 and (e) HC-8

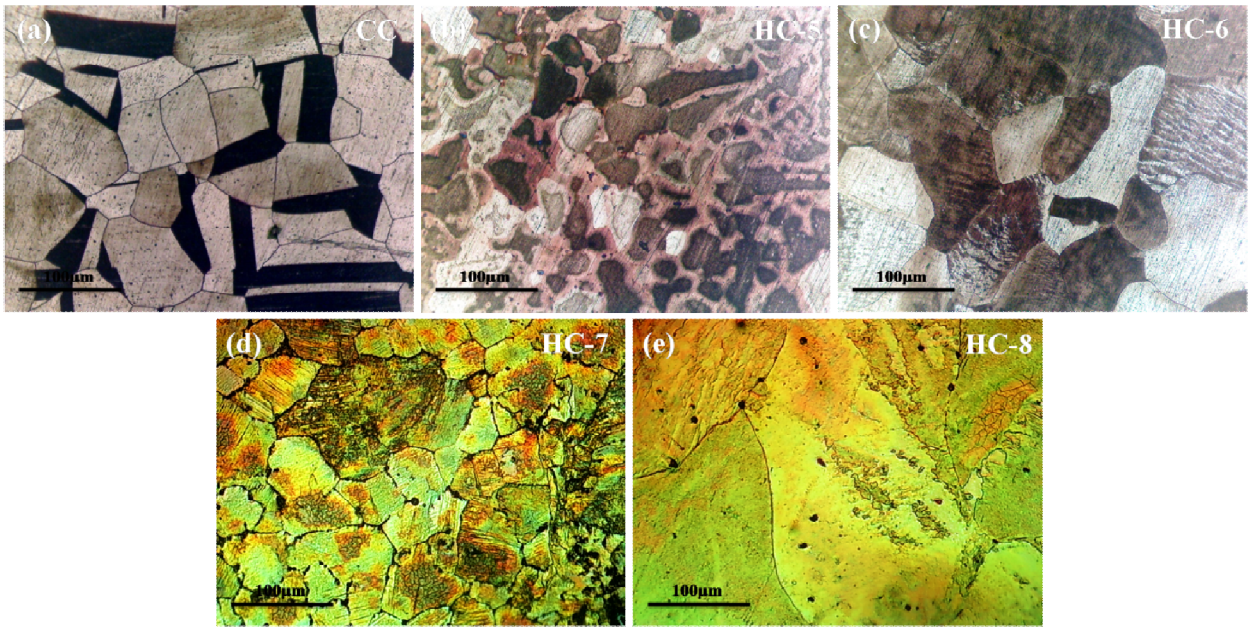

Fig.4.12. Microstructure of (a) CC, (b) HC-5, (c) HC-6, (d) HC-7 and (e) HC-8

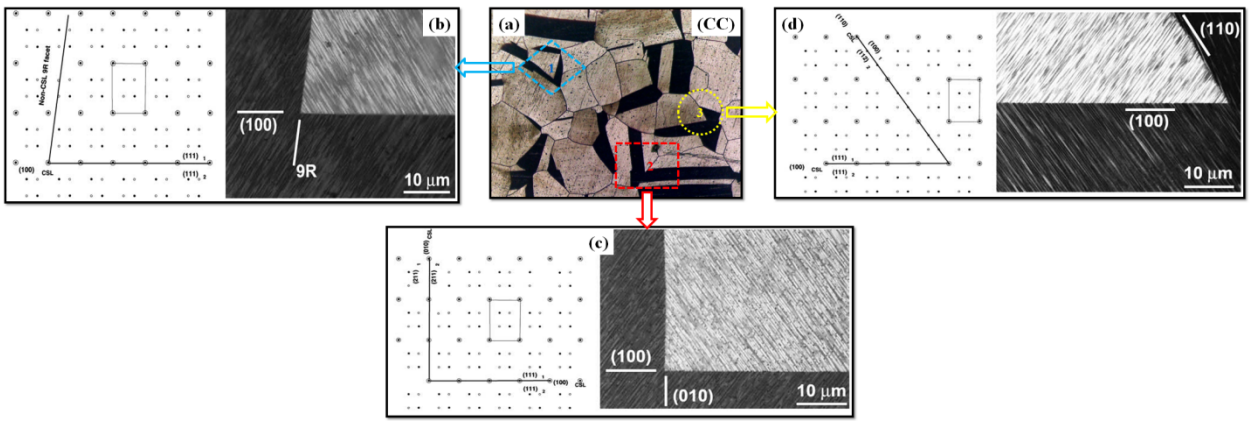

Fig.4.13. (a) Microstructure of CC and sections of Σ3 CSL at right angles to the {110} gradient axis with position of various facets and micrograph of intersections of $(100)_{CSL}$ with other facets (b) $(100)_{CSL}$ and 9R facets, (c) $(100)_{CSL}$ and $(010)_{CSL}$ facets (d) $(100)_{CSL}$ and $(110)_{CSL}$ facets (Straumal et al., 2006)

Figures 4.14 (a) to (d) show the HR-SEM microstructure of the developed hybrid composites i.e. HC-5, HC-6, HC-7, and HC-8, respectively. It is observed from Fig. 4.14 that the ceramic-reinforced particles are visible and fairly well distributed in the copper matrix. Quite agglomeration of the reinforcing materials in the copper matrix is also observed in HR-

SEM micrograph of HC-1 as shown in Fig. 4.14 (a). Figure 4.14 also reveals that the development of porosity that can be seen in the HR-SEM micrograph of hybrid composites. However, the presence of interface reaction is not observed in the HR-SEM micrograph of the hybrid composites as shown in Fig. 4.14.

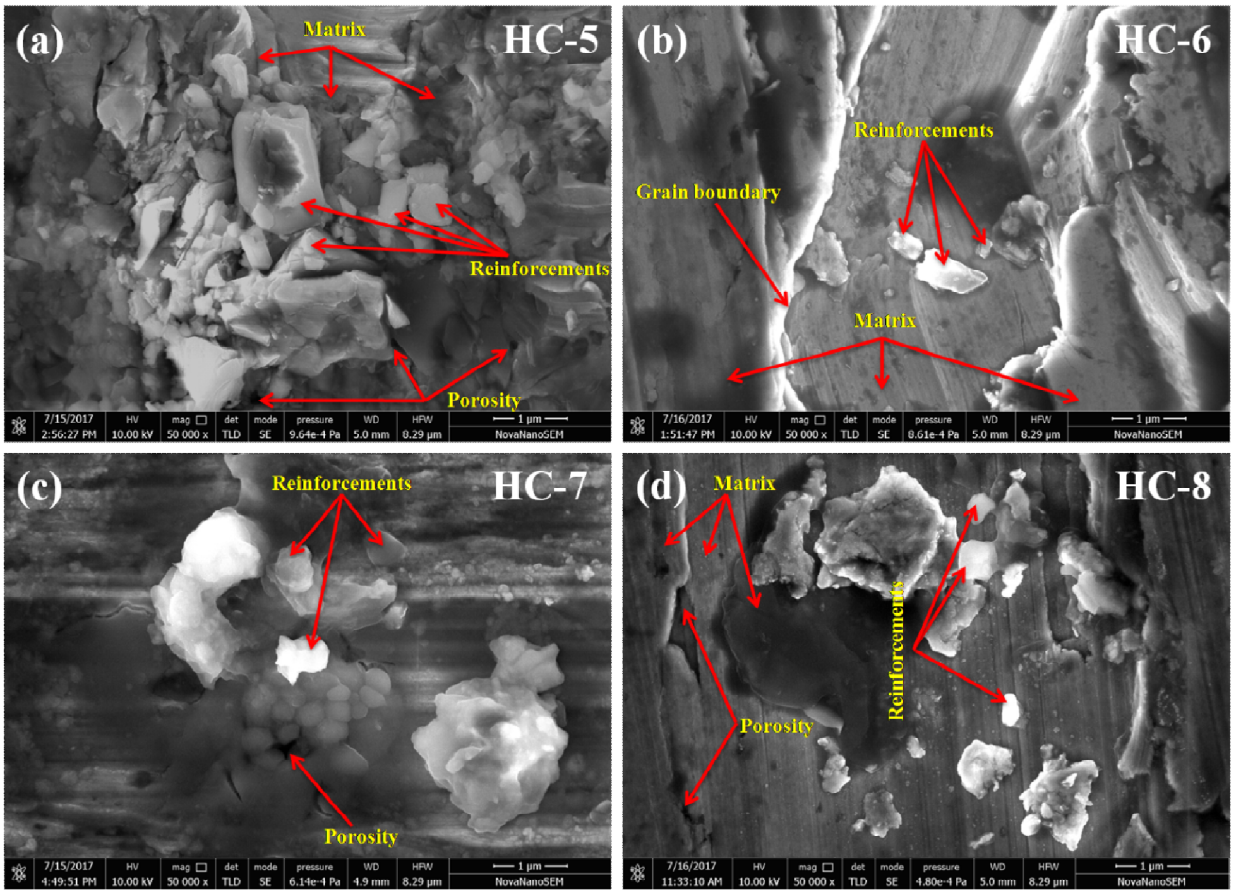

Fig.4.14. HR-SEM micrograph of (a) HC-5, (b) HC-6, (c) HC-7 and (d) HC-8

Figure 4.15 (a) to (e) shows the HR-SEM morphology of CC, HC-5, HC-6, HC-7 and HC-8 with selected area for corresponding color dot mapping, shown in Figs. 4.15 (a') to (e') and respective EDAX spectrum as revealed in Figs. 4.15 (a") to (e"). Figure 4.15 (a') shows the color dot mapping of the selected area in HR-SEM micrograph of CC that does not

display the additional color dots apart from the oxygen and copper. The presence of oxygen and copper in terms of weight and atomic percentage is reported in EDAX spectrum as shown in 4.15 (a''). The color coding of each elements with their percentage are highlighted on the top right corner of the respective color dot mappings, as shown in Figs. 4.15 (b') to (e'). However, corresponding EDAX spectrum of the materials reveals the significant presence of the reinforcing elements with their weight and atomic percentage, as shown in Figs. 4.15 (b'') to (e''). From the EDAX spectrum, it is observed that the weight and atomic percentage of B and C elements increases as the reinforcing percentage of B_4C in copper increases from 0 to 1.5 wt%.

Figure 4.16 (a) shows the HR-XRD pattern of CC, HC-5, HC-6, HC-7, and HC-8. The results have verified with joint committee powder diffraction standards (JCPDS) data file. It has been observed that copper-based hybrid composites hold all the original peaks of copper, and no supplementary peak found in the diffraction spectrum. However, HC-5 and HC-6 showed few copper oxide peaks including copper peaks. The peak broadening was observed in the enlarged view of diffraction plane (222) at diffraction angle of $2\theta=95.097^{o}$ as shown in Fig. 4.16 (b). It may be due to the effect of ceramic-reinforcement in the copper matrix. It was also observed that as the percentage of B_4C increases from x = 0 to x = 1.5 wt%, the peak shifted to the left and become broader as compared with CC peak.

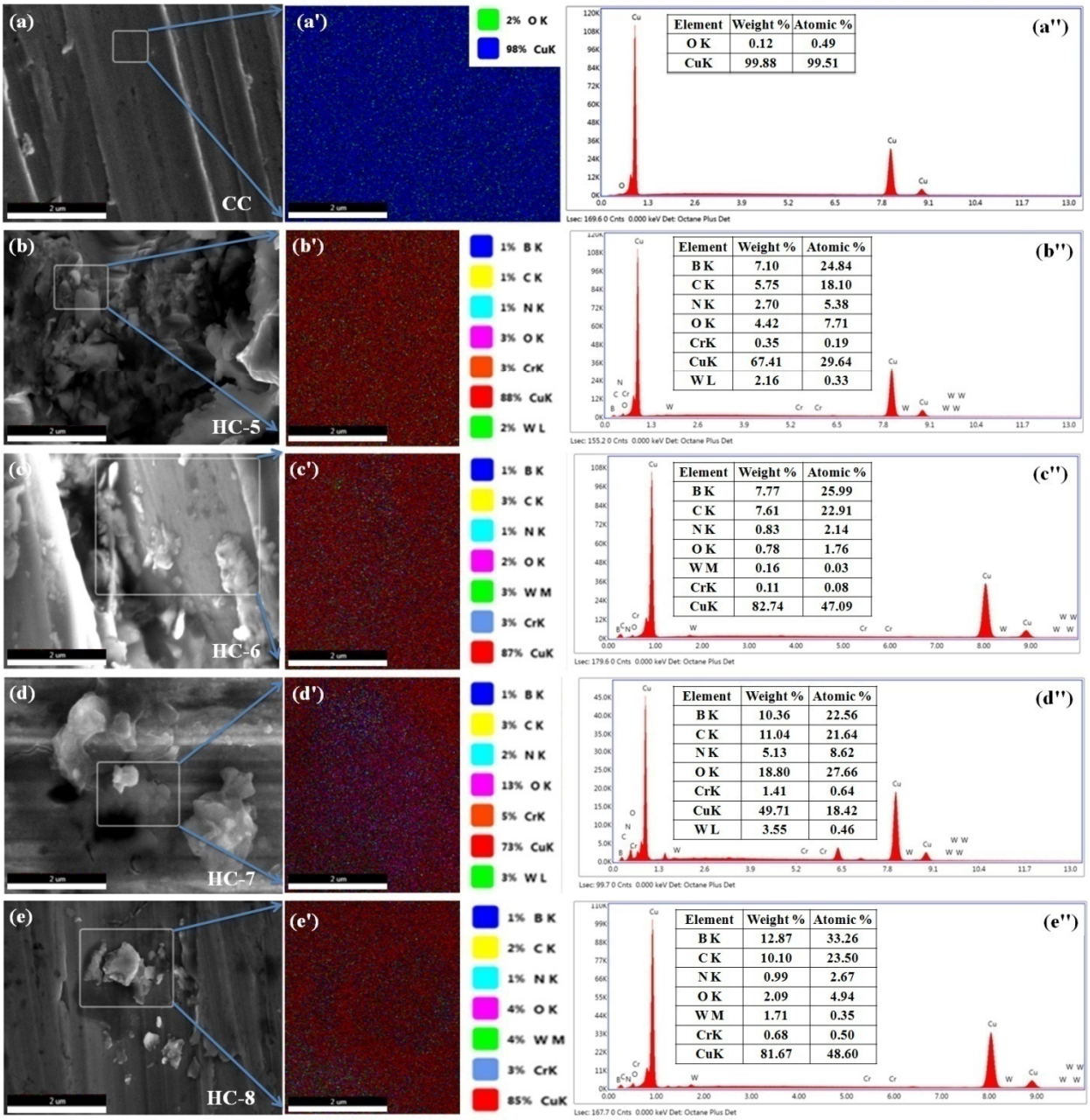

Fig.4.15. HR-SEM morphology of (a) CC, (b) HC-5, (c) HC-6, (d) HC-7, (e) HC-8, corresponding color dot mapping with color coding (a')-(e') and respective EDAX spectrum with report (a")-(e")

Table 4.3 shows the details of peak positions, diffraction planes, and their respective FWHM. Increase in FWHM indicates the decrease in crystallite size as shown in Table 4.4.

Figure 4.17 shows the effect of wt. % of B_4C on FWHM of the HRXRD peaks. It was observed that as the wt% of B_4C increases up to 1.0 wt%, the FWHM increases up to 0.2478º, but it comes down to 0.1637º when the wt% of B_4C goes to 1.5 wt%.

Williamson–Hall (W–H) determine (Williamson, 1953) the FWHM (β) of different Bragg peaks, as shown in Fig. 4.18, is carried out to know the source of the anomalous broadening of HR-XRD Bragg peaks due to addition of different wt% of B_4C with exclusion of $K\alpha_2$ involvement and instrumental broadening effects. Figure 4.18 shows the W-H plot, a relation between $\beta \cos\theta/\lambda$ and $\sin\theta/\lambda$, where θ is the Bragg's angle.

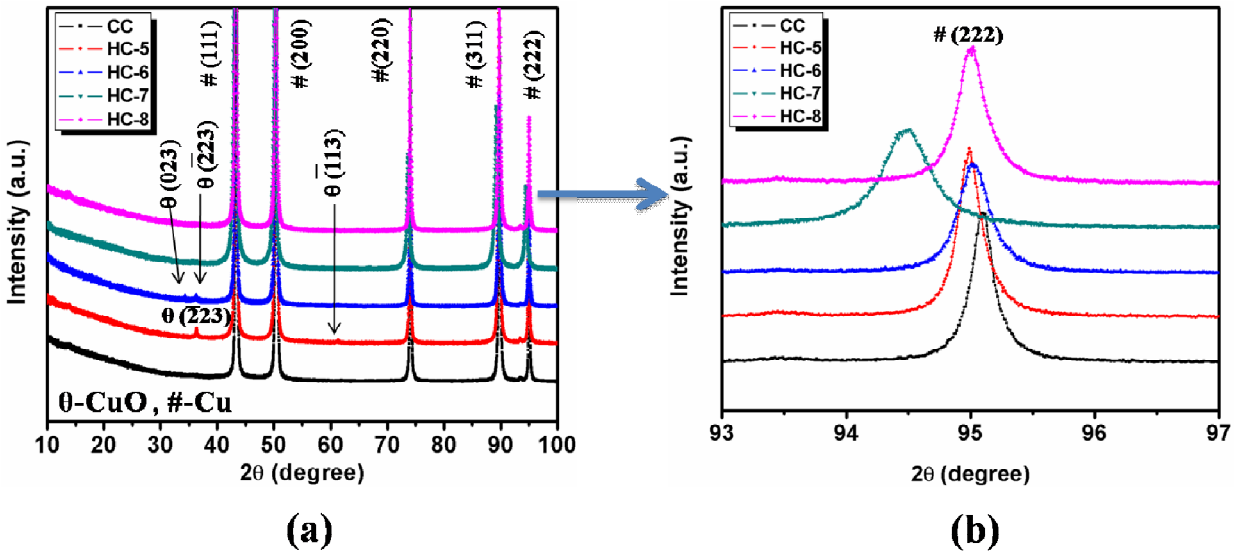

Fig.4.16. (a) HR-XRD pattern of CC and developed copper hybrid composites, (b) HR-XRD Bragg peak broadening (at 2θ = 95.097 degree)

Table 4.3. Details of the FWHM of the tertiary reinforced developed copper-based hybrid composites with their respective peak positions

Peak Position (2θ-deg.)	Diffraction Planes	FWHM (β-deg.) of CC	FWHM (β-deg.) of HC-5	FWHM (β-deg.) of HC-6	FWHM (β-deg.) of HC-7	FWHM (β-deg.) of HC-8
43.383	(111)	0.1489	0.1492	0.1548	0.2478	0.1637
50.442	(200)	0.2313	0.2535	0.2517	0.3812	0.2345
74.123	(220)	0.1714	0.2505	0.2549	0.3936	0.2064
89.849	(311)	0.2920	0.3014	0.3878	0.5424	0.3422
95.097	(222)	0.2026	0.2134	0.2520	0.3824	0.2417

Table 4.4. Details of the crystallite size and strain of the cast copper and tertiary reinforced developed copper-based hybrid composites

Samples	Strain	Size (nm)
CC	0.00068	116.67
HC-5	0.00139	68.20
HC-6	0.00236	56.10
HC-7	0.00273	35.09
HC-8	0.00247	51.06

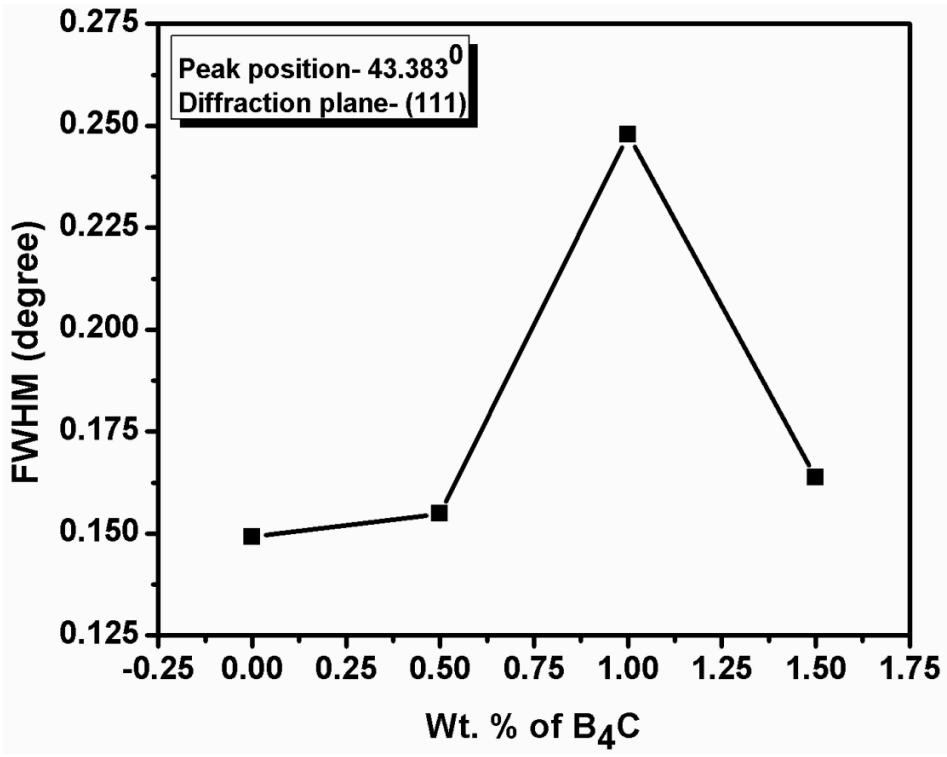

Fig.4.17: Variation of the FWHM with wt. % of B_4C

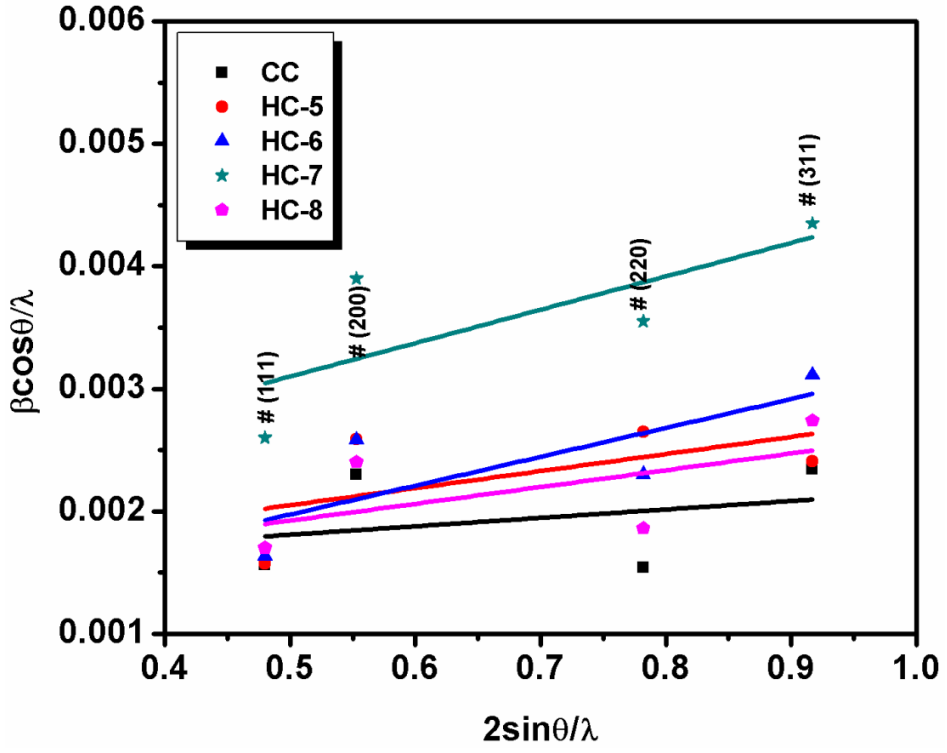

Fig.4.18. Williamson–Hall (W-H) plot for the CC, HC-5, HC-6, HC-7, and HC-8

4.3.2. Physical properties

Table 4.5 shows the detail variation of experimental density, theoretical density, relative density, porosity and electrical conductivity of CC, HC-5, HC-6, HC-7 and HC-8. From the Table 4.5, it is observed that the experimental density of hybrid composites is lower compared with the CC. It is also observed that the experimental density of the copper hybrid composites decreases with increasing wt% of B_4C reinforcement with constant wt% of WC and BN into the copper matrix. Some variation in experimental density of hybrid composites is also observed, HC-7 exhibits the optimum experimental density among all the hybrid composites however, least experimental density is observed in HC-8.

Table 4.5 also shows the theoretical density of the hybrid composites are lower as compared with CC and it displays a decreasing pattern with increasing content of B_4C reinforcement in matrix. The porosity and relative density of the hybrid composites are found higher and lower respectively compared to CC. The porosity of the hybrid composites increases with increasing B_4C reinforcement content however, the relative density of hybrid composites decreases with increasing content of B_4C. HC-7 shows the exceptional result of the experimental, theoretical, relative density and porosity among all the hybrid composites.

Table 4.5 shows the electrical conductivity of CC, HC-5, HC-6, HC-7 and HC-8. In the present study, electrical conductivity is reported in terms of the percentage international annealed copper standards (% IACS). From the Table 4.5, it is observed that the electrical conductivity of hybrid composites is lower than CC. It is also observed that the electrical conductivity decreases with increasing in wt% of B_4C with constant wt% of WC and BN in copper matrix. The electrical conductivity decreases from 85 (of CC) to 43 % IACS (of HC-5) with the addition of 1.5 wt% WC and 1 wt% BN with zero wt% of B_4C into the copper

matrix. Moreover, the 43 % IACS electrical conductivity of HC-5 decreases to 32 % IACS (of HC-6) when wt% of B_4C increases from 0 to 0.5 with the same amount of WC and BN. Further, decrease in electrical conductivity from 32 (of HC-6) to 25 % IACS (of HC-7) and from 25 (of HC-7) to 19 % IACS (of HC-8) are observed when the wt% of B_4C increases from 0.5 to 1.0 and 1.0 to 1.5, respectively, with similar amount of WC and BN. Loss of 49.41, 62.35, 70.58, and 77.64 % IACS are observed in HC-5, HC-6, HC-7, and HC-8, respectively, with comparison to CC.

Table 4.5. Variation of experimental density, theoretical density, relative density, porosity and electrical conductivity of CC, HC-5, HC-6, HC-7 and HC-8

Materials	**Experimental density (ED) ($g.cm^{-3}$)**	**Theoretical density (TD) ($g.cm^{-3}$)**	**Relative density (RD) (%)**	**Porosity (%)**	**% IACS**
CC	8.33± 0.25	8.96	92.97± 0.25	~7	82±5
HC-5	7.82± 0.25	8.95	87.37± 0.25	~12	43±3
HC-6	7.59± 0.2	8.92	85.09± 0.2	~15	32±2
HC-7	8.05± 0.29	8.89	90.55± 0.29	~9	25±4
HC-8	7.43± 0.32	8.86	83.86± 0.32	~16	19±2

4.3.3. Mechanical properties

Figure 4.19 (a) shows the behavior of the Brinell hardness of CC, HC-5, HC-6, HC-7, and HC-8. Hybrid composites exhibit the higher hardness than CC as shown in Fig. 4.19 (a). It is also observed that the hardness of hybrid composites increases with increase in B_4C content. The hardness of hybrid composites only increases up to 1.0 wt% of B_4C content and

further it decreases as B_4C content goes to 1.5 wt%. It is observed that the HC-7 shows the optimum Brinell hardness however, HC-5 shows least hardness among all hybrid composites. By comparing with CC, percentage enhancement in Brinell hardness of HC-5, HC-6, HC-7 and HC-8 is 11.92, 25.71, 53.76 and 38.18 respectively.

The behavior of compressive strength of CC, HC-5, HC-6, HC-7 and HC-8 is shown in Fig. 4.19 (b). From the Fig. 4.19 (b), it is observed that the compressive strength of the developed hybrid composites is higher than CC. The percentage enhancements in the compressive strength are 24.65, 32.87, 52.05, and 53.42% of HC-5, HC-6, HC-7 and HC-8 respectively with respect to CC. It is also observed that the compressive strength of hybrid composites increases as the reinforcement content of B_4C increases from 0 to 1.5 wt%. Here, HC-8 exhibits the highest compressive strength, while, HC-5 shows the least compressive strength among all hybrid composites.

Figure 4.19 (c) shows the behavior of ultimate tensile strength (UTS) of CC, HC-5, HC-6, HC-7 and HC-8. Hybrid composites show the higher UTS value compared with CC as shown in Fig. 4.19 (c). An increase in UTS values of hybrid composites is observed with increasing in B_4C content from 0 to 1.0 wt% and further it decreases when B_4C content increases to 1.5wt% as shown in Fig. 4.19 (c). An improvement of 16.2, 27.6, 50.4, and 39.0% in UTS is observed for HC-5, HC-6, HC-7 and HC-8 compared with CC respectively. HC-7 displays the highest UTS among all materials however; CC shows the least UTS. Though, among hybrid composites HC-1 exhibits the lowest UTS.

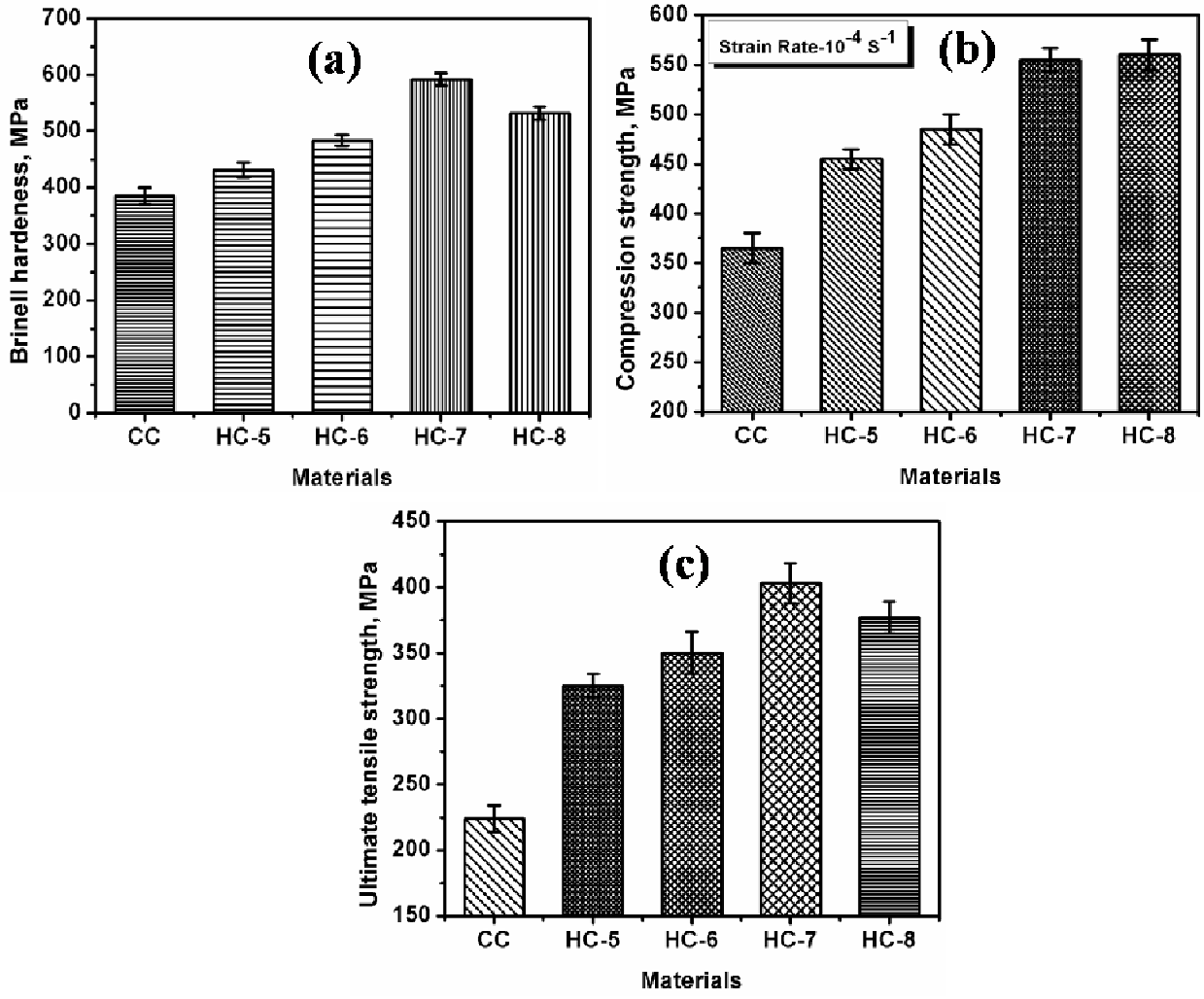

Fig.4.19. The variation of properties of tertiary reinforced hybrid composites (a) Brinell hardness (b) Compression strength, (c) Ultimate tensile strength

Figures 4.20 (a) to (e), and 4.21 (a) to (e) shows the SEM morphology of fractured surface of CC, HC-5, HC-6, HC-7 and HC-8 at 70 and 2000× magnification respectively. Figures 4.20 (a) to (e) reveal the typical fractures involve during tensile test. It is observed that the CC has a cup type of failure as shown in Fig. 4.20 (a). However, the fracture face of hybrid composites shows approximately flat surfaces as shown in Fig. 4.20 (b) to (e). The fracture surface of the HC-7 at 70× magnifications shows the maximum flatness as observed in Fig. 4.20 (d), however least flatness is observed in CC. Morphology of the CC at 2000×

magnification reveals larger size of dimples as shown in Fig. 4.21 (a). Whereas, the micrograph of the fractured surface of HC-5, HC-6, HC-7 and HC-8 at 2000× magnification shows smaller dimples compared with CC, which as shown in Fig. 4.21 (b) to (e). The fractography of the highest strengthened HC-7 shows a unique geometry, such as strong networking-like spider nets, as shown in Fig. 4.21 (d), with almost zero micro voids.

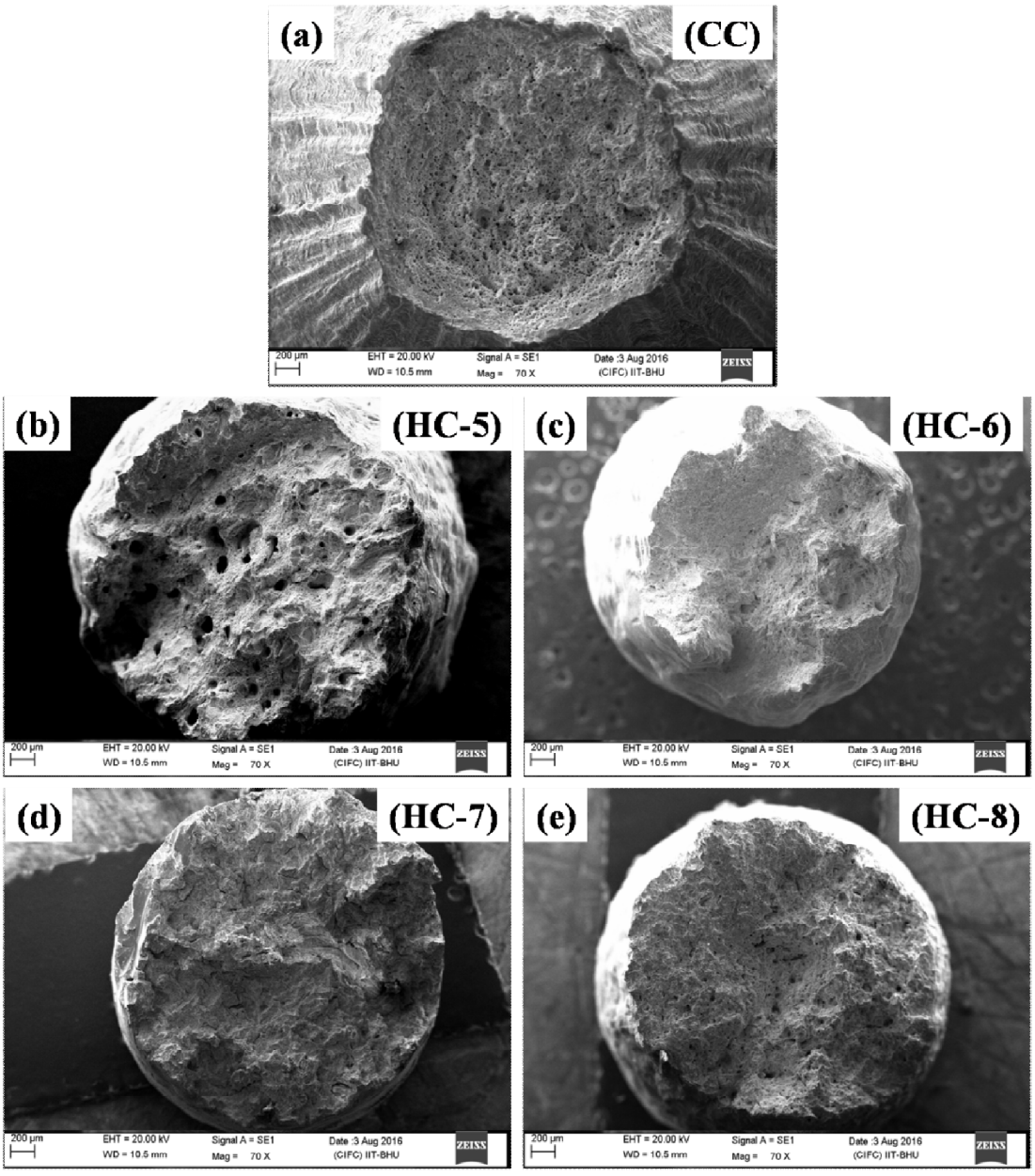

Fig.4.20. The SEM micrograph of fractured surface of (a) CC, (b) HC-5, (c) HC-6, (d) HC-7, and (e) HC-8 at 70× magnification

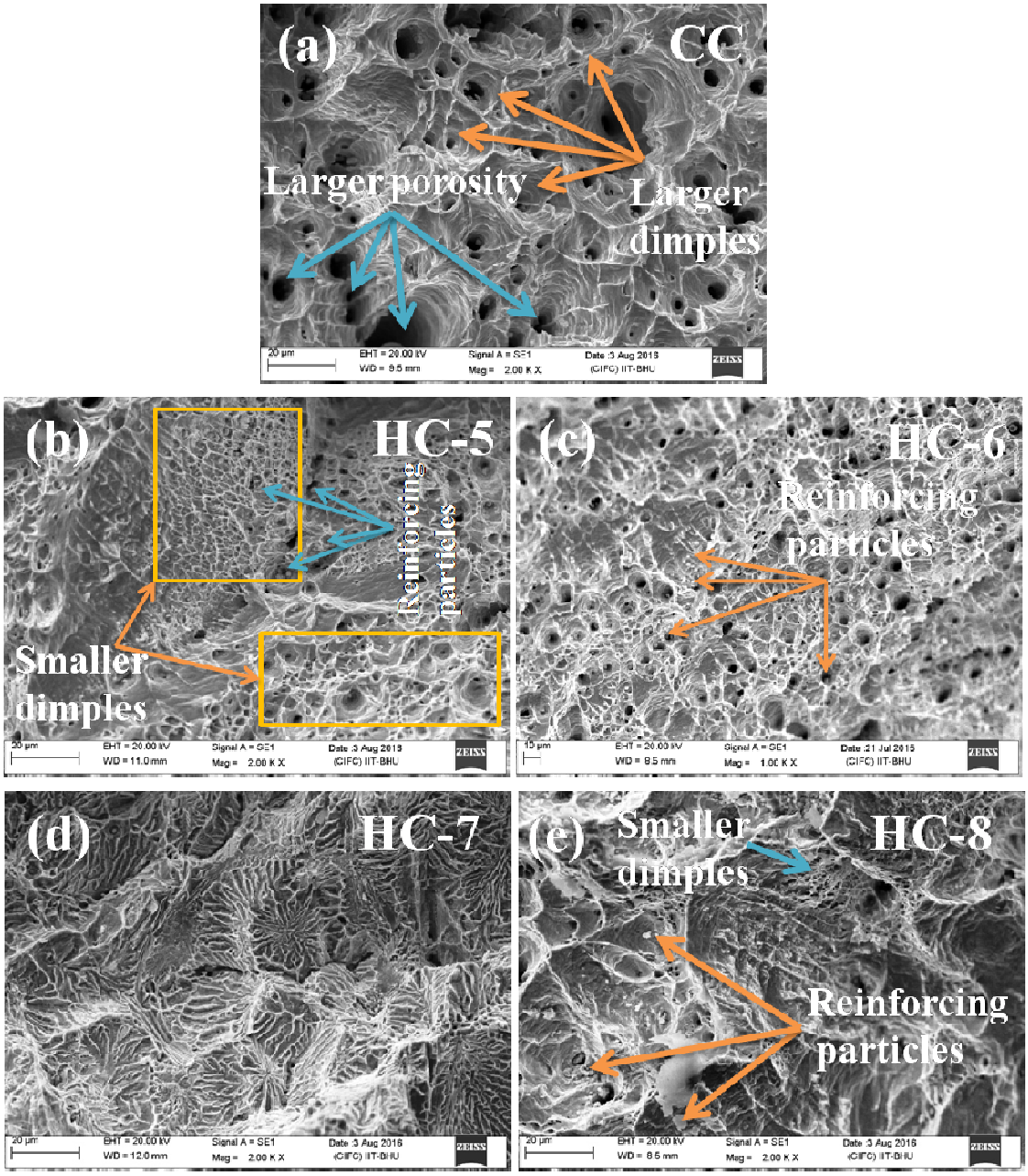

Fig.4.21. The SEM micrograph of fractured surface of (a) CC, (b) HC-5, (c) HC-6, (d) HC-7, and (e) HC-8 at 2000× magnification

Figures 4.22 (a) to (e) show the EDAX spectrum of the fracture surface of CC, HC-5, HC-6, HC-7 and HC-8, respectively. Fracture faces of the materials are investigated through EDAX to observe the significant presence of reinforcing particles in the materials. In the EDAX spectrum of CC, additional intensity peaks are not found other than oxygen and

copper intensity peak. The EDAX spectrum of the entire hybrid composites does not show the intensity peak of boron. Though, intensity peaks of almost all the reinforcing elements are observed in the entire EDAX spectrum of hybrid composites. In the EDAX spectrum of the HC-6 and HC-7 the intensity peak of chromium is not observed in the particular region, while the intensity peaks of other elements are observed as shown in Fig. 4.22 (c) and (d).

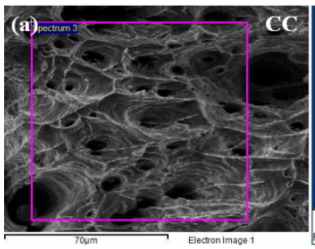

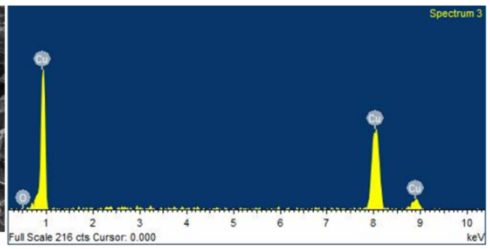

Element	Weight%	Atomic%
O K	0.23	0.90
Cu K	99.77	99.10
Totals	100.00	

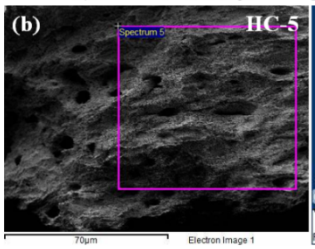

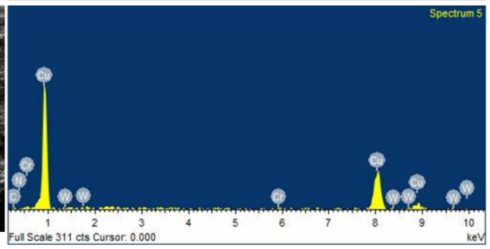

Element	Weight%	Atomic%
C K	18.87	49.53
N K	5.92	13.31
Cr K	0.73	0.46
Cu K	75.01	37.12
W M	0.24	0.04
Totals	100.00	

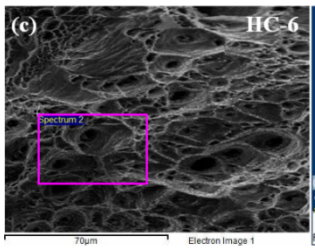

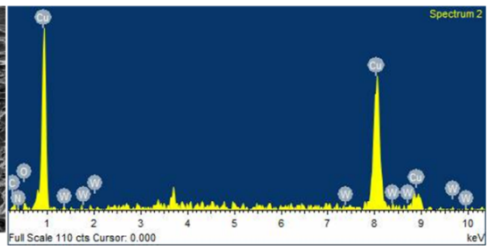

Element	Weight%	Atomic%
C K	22.92	52.94
N K	6.40	12.67
O K	2.75	4.76
Cu K	67.85	29.62
W M	0.09	0.01
Totals	100.00	

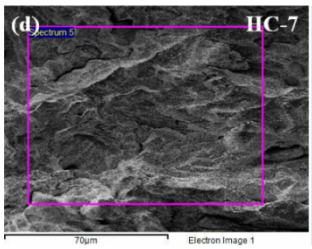

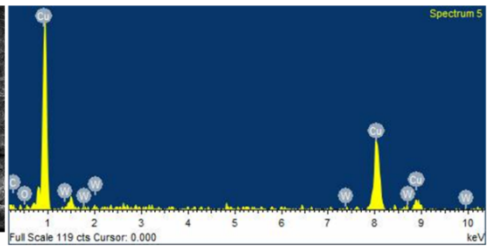

Element	Weight%	Atomic%
C K	26.75	53.63
N K	13.56	23.32
O K	0.59	0.89
Cu K	58.16	22.04
W M	0.93	0.12
Totals	100.00	

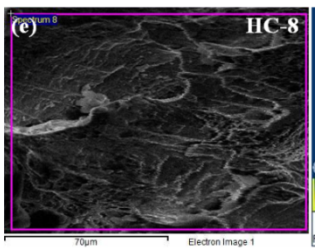

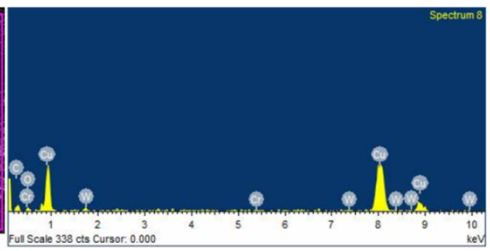

Element	Weight%	Atomic%
C K	29.22	61.44
N K	4.41	7.96
O K	3.61	5.69
Cr K	0.39	0.19
Cu K	62.12	24.69
W M	0.26	0.04
Totals	100.00	

Fig.4.22. The EDAX spectrum of fractured surface of (a) CC, (b) HC-5, (c) HC-6, (d) HC-7, (e) HC-8

4.4. Comparison of physical and mechanical properties of binary and tertiary reinforced copper-based hybrid composites

The comparative study of the physical and mechanical properties of binary and tertiary reinforced copper-based hybrid composites have been done and its results are given in the Table 4.6. From the Table 4.6, it is observed that the experimental density, theoretical density and relative density of entire hybrid composites are lower compared with CC. However, the porosity developed in both the hybrid composites is higher than porosity developed in CC. While comparing binary and tertiary hybrid composites, the experimental density, relative density and porosity of the tertiary hybrid composites are better as compared with binary reinforced hybrid composites. However, theoretical density of the tertiary hybrid composites is poor than binary reinforced hybrid composites. Table 4.6 also exhibits the better Brinell hardness, UTS and compressive strength of all the developed hybrid composites as compared with CC. It is also observed the significantly good mechanical properties of the tertiary reinforced hybrid composite as compared with binary reinforced hybrid composites as given in Table 4.6. The electrical conductivity of both binary and tertiary hybrid composites is lower than the electrical conductivity of CC. While, comparing the electrical conductivity of binary and tertiary reinforced hybrid composites, it is found that he electrical conductivity of binary reinforced hybrid composites is higher than tertiary reinforced hybrid composites. So, overall it can inferred that all the developed hybrid composites have better properties compared with CC and tertiary reinforced hybrid composites show its best in almost all the properties except electrical conductivity.

Table 4.6. Comparative details of physical and mechanical properties of binary and tertiary reinforced copper-based hybrid composites

Materials	E.D. ($g.cm^{-3}$)	T.D. ($g.cm^{-3}$)	R.D. (%)	Porosity (%)	BHN (MPa)	UTS (MPa)	Compressive strength (MPa)	%IACS
CC	8.33±0.25	8.96	92.97±0.25	~7	385±15	224±10	343±8	82±5
HC-1	7.55±0.2	8.95	84.36±0.2	~15	445±10	270±12	395±7	25±2
HC-2	7.67±0.15	8.94	85.80±0.15	~14	492±12	335±15	427±10	39±3
HC-3	7.45±0.3	8.92	83.52±0.3	~16	520±10	345±10	464±10	20±2
HC-4	7.88±0.25	8.89	88.64±0.25	~11	558±15	385±15	507±9	55±4
HC-5	7.82±0.25	8.95	87.37±0.25	~12	431±13	325±9	455±10	43±3
HC-6	7.59±0.2	8.92	85.09±0.2	~15	484±9	350±16	485±15	32±2
HC-7	8.05±0.29	8.89	90.55±0.29	~9	592±11	403±15	555±12	25±4
HC-8	7.43±0.32	8.86	83.86±0.32	~16	532±12	377±12	560±16	19±2

4.5. Discussion

The various copper-based hybrid composites are developed using the stir-casting technique. The developed hybrid composites are divided into two categories, binary reinforced and tertiary reinforced copper-based hybrid composites. Binary hybrid composites are developed by utilizing the two different ceramic reinforcements in single copper metal matrix. However, the tertiary hybrid composites are developed by incorporating three different ceramic reinforcements in copper matrix. Where, the chromium is added to both kinds of hybrid composites to improve the wettability of reinforcing particles in the copper matrix. Before adding the ceramic reinforcements in the copper matrix to develop the hybrid composites, they are analyzed using SEM instruments equipped with EDAX and results are

shown in Figs. 4.1 to 4.3. Figures 4.1 (a) to (f) show the morphology of the WC, Cr, B_4C, Al_2O_3, BN and ZrO_2, respectively. Where, almost all the reinforcing particles are homogeneous, regular and non-agglomerated except ZrO_2, it shows some agglomeration as shown in Fig. 4.1 (f). The size of entire reinforcing particles varies in the range of 1-50 µm which are frequently used for developing composites, the histogram of particles size distribution are shown in Figs. 4.2 (a) to (f). The particle size of reinforcements is one of the major parameter to observe the changes in behavior of materials. Chawla (2012) has been reported that the appropriate size of reinforcement particle should vary in the range of 1.0 - 50.0 µm during incorporation in the metal matrix. In addition to this, to ensure the purity of reinforcing particles the EDAX analysis is accomplished and their spectrum is shown in Figs. 4.3 (a) to (f). EDAX spectrum of entire reinforcing phase display the intensity peaks of their respective elements only. However, EDAX spectrum of chromium shows the carbon intensity peak, it may be attributed to the carbon tape used to mount the sample for EDAX characterizations.

4.5.1. Binary reinforced copper-based hybrid composites

The developed binary reinforced hybrid composites are subjected to its microstructural study through EDAX, HR-SEM and XRD and their results are depicted in Figs. 4.4, 4.5 and 4.7 respectively. Figures 4.4 (a) to (e) show the EDAX spectrum of the CC and binary reinforced hybrid composites i.e. HC-1, HC-2, HC-3, and HC-4 respectively. The entire EDAX spectrums of the hybrid composites show the intensity peaks of respective reinforcing materials with their weight and atomic percentage in the table. The intensity peaks of oxygen and copper are only observed in the EDAX spectrum of the CC with their

weight and atomic percentage as shown in Fig. 4.4 (a). The presence of oxygen intensity peak may be attributed to oxidation of copper with residual oxygen in the furnace. In the EDAX spectrum of HC-1 and HC-3, the weight and atomic percentage of oxygen and zircon increases as the weight percentage of ZrO_2 increases, as shown in Fig. 4.4 (b) and (d). This may be due to increase in the oxygen and zircon atom form of the ZrO_2. However, the oxygen intensity peak is not observed in the EDAX spectrum of the HC-2, as shown in Fig. 4.4 (c). It may be due the absence of oxygen element in the selected area for characterization. While, Fig. 4.4 (e) shows the EDAX spectrum of HC-4 where, the intensity peak of oxygen and it's low weight and atomic percentage is observed including other element. Silicon intensity peak is also observed in the EDAX spectrum of HC-2 and HC-4; it may be attributed to the presence of silica in the selected area for characterization. During the polishing of hybrid composites with silica emery papers where, the harder silica may embedded into the surface of hybrid composites.

In addition to this, the EDAX analysis of binary reinforced hybrid composites is followed by HR-SEM to identify the distribution of reinforcing phase in the copper matrix, as shown in Figs. 4.5 (a) to (c). Figures 4.5 (b) and (c) show very nicely the presence of reinforcing particles and its homogeneous distribution in the copper matrix. However, the evidence of any kind of foreign element in CC is not present only smooth surface of copper matrix observed as shown in Fig. 4.5 (a). The micrograph of the hybrid composites reveals that the reinforcing phases are entrapped in the matrix by mechanical bonding where, WC and ZrO_2 reinforcing particles can be observed in the micrograph of HC-3 as shown in Fig. 4.5 (b) and WC and Al_2O_3 in the micrograph of HC-4, as depicted in Fig. 4.5 (c). The reinforcing particle can be easily observed in the enlarged view as shown in Fig. 4.5 (b') and

(c') which reveals structural morphology of the respective reinforcing particle in matrix i.e. monoclinic structure of ZrO_2 in HC-3 and trigonal structure of Al_2O_3 in HC-4.

In support of above results, the color mapping is also carried out during the HR-SEM investigation to assure the developed hybrid composites contain the reinforcing particles as revealed in Fig. 4.6. Figure 4.6 (a') exhibits the color dot mapping of CC, that display the color dots of O and Cu only with its weight and atomic percentage as depicted in 4.6 (a''). The occurrence of O peak may be due to the oxidation of copper with the residual oxygen in furnace at high temperature during casting. However, HR-SEM morphology of developed hybrid composites exhibit the distribution of all reinforcing materials and their presence, which is confirmed by their respective color dot mapping of the selected area. Color dot mapping of respective hybrid materials shows the significant presence of different reinforcing elements and its matrix, which are coded with different colors. The color coding of each elements with their percentage are highlighted on the top right corner of the respective color mappings, as shown in Fig. 4.6 (b') to (e'). However, corresponding EDAX spectrum of the materials reveals the significant presence of the reinforcing elements with their weight and atomic percentage, as shown in 4.6 (b'') to (e''). From the EDAX spectrum as shown in Fig 4.6 (b'') to (e''), it is observed that the weight and atomic percentage of Zr and Al elements increases as the reinforcing content of ZrO_2 and Al_2O_3 in copper increases from 1 to 2 wt%. This investigation confirms that the developed hybrid composites contain the reinforcing particles.

The XRD spectrum of the CC and binary reinforced hybrid composites are shown in Fig. 4.7, and the results have been compared with JCPDS data. The XRD pattern shows the hybrid composites contain all the original peaks of copper only, no others peaks are found in

the diffraction pattern. So, it can be inferred from the XRD pattern that during the development of binary reinforced hybrid composites, no reaction between copper matrix and ceramic reinforcements take place. If any new phase formation is there and amount of reinforcement is less than 5 wt% that can not be detected by the XRD (Samal et al., 2013). However, the Bragg peak intensity and peak broadening are found different from CC that may be attributed to the reinforcement of ceramic particles to the copper matrix. The full width at half maxima (FWHM) of XRD Bragg peak of the materials is shown in the Table 4.1. From the Table 4.1, it is observed the FWHM of XRD Bragg peak in hybrid composites is higher compared with CC; it means that the crystallite size of hybrid composites decreases with increasing content of ceramic reinforcement into the copper matrix. The decrease in crystallite size of the hybrid composites plays a significant role on the strengthening of the materials .The broadening of diffraction peaks are featured due to the internal strain developed due to micro distortion of the lattice on addition of ceramic reinforcement in copper matrix (Chen et al., 2018; Wang et al., 2018). Kumar et al. (2017) have made the similar study for X-ray diffraction pattern. In which, there was no phase changes observed in XRD pattern but a little peak shift and broadening of Bragg diffraction peak were observed. It was also observed that the average crystallite size decreases as the Bragg peak broaden. Bagheri (2016) has also reported that copper with different percentage of reinforcement shows the broader diffraction peak and decreased intensity of peak with increasing reinforcement in copper matrix. It is attributed to the reduction in crystallite size and increase in internal strain of copper. FWHM of the XRD Bragg peak in Al_2O_3 reinforced hybrid composites is higher compared with FWHM of CC and ZrO_2 reinforced hybrid composites as

given in Table 4.1. Thus, it can be concluded that the developed hybrid composites contain the reinforcing materials.

The microstructural study of the binary reinforced hybrid composites are followed by physical properties observation as shown in Table 4.2. It shows the variation of the experimental, theoretical, relative density, porosity and electrical conductivity of CC and binary ceramic reinforced copper hybrid composites. It is observed that the experimental density of the developed hybrid composites is lower compared with CC. It may be attributed to the reinforcement of lower density materials (Chandrakanth et al., 2010) such as Al_2O_3 (3.95 $g.cm^{-3}$) and ZrO_2 (5.68 $g.cm^{-3}$) with Cr (7.19 $g.cm^{-3}$) to the copper matrix. It may also attribute to the development of porosity in the hybrid composites due to some possible agglomeration as shown in Fig. 4.5 on increasing the reinforcing content. The porosity of the materials is reported in the Table 4.2. In addition to this, the variation in shape, size and crystal structure of the reinforcing materials may also develop some defects like-voids and porosity which lower the density of hybrid composites (Callister, 2007).

The electrical conductivity of the developed materials is also investigated and the results are reported in the Table 4.2. Where, the electrical conductivity of the developed materials is reported in percentage of international annealed copper standard (% IACS). It is observed that electrical conductivity of hybrid composites is lower than CC as shown in Table 4.2. It may be attributed to the addition of non-conducting nature of the ceramic reinforcing materials such as WC, ZrO_2 and Al_2O_3 compared with conducting nature of copper. The variation in electrical conductivity is also observed with variable content of ceramic reinforcements. It is observed that as the percentage of ZrO_2 increases from 0 to 2 wt% with constant wt% of WC and Cr, the conductivity decreases from 82 to 20 % IACS.

However, with increasing content of the Al_2O_3 from 0 to 2 wt% with the same wt% of WC and Cr, the conductivity decreases from 82 to 55 % IACS. Here, it observed that the Al_2O_3 based hybrid composite shows a better conductivity compared with ZrO_2 reinforced. It may be attributed to the inherent properties of Al_2O_3 grade 6 i.e. A6, that has good electrical properties compared with its other grades and ZrO_2. So, the improvement in the electrical conductivity of HC-2 and HC-4 are envisaged. The electrical conductivity of CC, HC-1, HC-2, HC-3 and HC-4 are 82, 25, 39, 20 and 55 % IACS respectively.

Fig. 4.8 (a) exhibits the Brinell hardness of the binary reinforced hybrid composites is higher than CC. Such improvement in hardness of hybrid composites is attributed to the higher hardness and elastic modulus of the Al_2O_3, ZrO_2, and WC reinforcement compared with its copper matrix. Where, normally the Al_2O_3, ZrO_2 and WC reinforcement share most of the load, when an external load is applied. It is also observed that there is increase in the hardness with increases in content of Al_2O_3 and ZrO_2, which reveals the good stability of reinforcing particles in copper matrix. This may also be attributed to the good interfacial contact between the reinforcing particles and copper matrix, can be observed in Fig. 4.5. In addition to this, proper distribution of the reinforcing particles in the matrix also influences the strengthening of the composite materials by restricting the grain growth (Rajkumar et al., 2011). Thermal mismatch between the reinforcing particles and the copper matrix also results in internal stresses which generate the dislocations leading to an increase in the dislocation density which ultimately contributes in enhancing the hardness of the composites as reported by Tabandeh et al. (2010). An improvement of 15.58, 27.79, 35.06, and 44.93 % in Brinell hardness of HC-1, HC-2, HC-3, and HC-4 are observed compared with CC, respectively.

The behaviour of compressive strength of CC and binary reinforced hybrid composites are shown in Fig. 4.8 (b). During compression test, the metal matrix composites deform primarily by two mechanisms, namely boundary slip deformation and matrix grain deformation (Lin et al., 2004). The compression strength of the developed hybrid composites is higher than CC as depicted in Fig.4.8 (b). It may be due to the reinforcement of ceramic materials with higher young modulus to the lower modulus of copper matrix, where the strengthening mechanisms such as Hall–Petch, load transfer effect and mismatch of elastic moduli of the matrix and reinforcing particle involves to improving the compressive strength of the hybrid composites materials (Casati et al., 2014). The particle size of the reinforcement also influences the compressive strength of the hybrid composites because large sized (μm) particles impede the plastic flow of the matrix more effectively than the smaller sized (nm) particles during compression (Lin et al., 2004). The considerable enhancement in compressive strength of Al_2O_3 reinforced copper hybrid composites (HC-2, HC-4) is observed compared with copper matrix and ZrO_2 reinforced hybrid composites (HC-1, HC-3). It can be attributed to significant grain refinement, presence of reasonably distributed harder particulates. In addition to this, strengthening arises from increase in dislocation density of the matrix because of different thermal expansion coefficients of the matrix and particles, load transfer from matrix to reinforcements/second phases and Orowan strengthening mechanism (Nguyen et al., 2010; Zhang et al., 2004; Hassan et al., 2003; Nguyen et al., 2008; Szaraz et al., 2007). Overall, Al_2O_3 reinforced hybrid composites have better compressive strength compared with others. With comparison to CC there is an improvement of compressive strength as 15.16, 24.48, 35.27, and 47.8 % in HC-1, HC-2, HC-3, and HC-4, respectively.

The behavior of ultimate tensile strength (UTS) of CC and binary reinforced hybrid composites is revealed in Fig. 4.8 (c) and it is observed that hybrid composites have higher UTS than CC. This significant improvement in UTS is owing to the high intrinsic stiffness and strength of the reinforcing phase like-ZrO_2, Al_2O_3 and WC, which avoid the shearing and rupture of the binary hybrid composites, and thus the Al_2O_3, ZrO_2 and WC act as efficient constraints to propagation of dislocations across the interface between copper matrix and reinforcements (Kim et al., 2013). However, higher UTS is achieved at the expense of ductility of copper matrix; it is a general trend in metal matrix composites due to lower ductility of the reinforcing phase such as WC, ZrO_2 and Al_2O_3 etc. (Tang et al., 2014). An enhancement of 20.53, 49.55, 54.01, and 71.87% in UTS is observed in HC-1, HC-2, HC-3, and HC-4 respectively as compared with CC. This enhancement in UTS may also be due to the superior hardness as discussed earlier and to the strong interfacial bonding between the reinforcement and copper matrix. Where, addition of Cr improves the wettability of the reinforcing phase by making a coating of it (Gautam et al. 2011). This lowers the surface tension and promotes superior wettability with molten copper matrix. Wettability is one of the dominating parameters to ensure good bonding between reinforcements and copper matrix (Ramesh et al., 2009), where, a good bonding between reinforcements and metal matrix always promotes a development in the UTS of hybrid composite materials.

The fracture surfaces of CC and binary reinforced hybrid composites are analyzed using SEM to identify the involvement of its fractured behaviors. Fractured surfaces are shown in Figs. 4.9 (a) to (e). It is observed that the hybrid composites display a different fractured morphology compared with CC as shown in Fig. 4.9. The development of larger dimple confirms the ductile fracture behavior of CC which is developed by the coalescences

of the cavity. The presence of the pores is also visible in the micrograph of fractured surface of CC as shown in Fig. 4.9 (a). However, the entire fractured surface morphology of binary reinforced hybrid composites show the smaller dimples compared with CC. Where, the smaller dimples confirm the brittle fracture behaviour of the hybrid composites. The reinforcing particles are also observed in the micrograph of fractured surface as shown by the arrow in the all micrograph of hybrid composites as shown in Fig. 4.9 (b) to (e). The reinforcing particles are entrapped in the cavity of the matrix materials. Therefore, these particles play a crucial role by not allowing quicker propagation of cracks in the materials. Hence, the hybrid materials have higher ultimate tensile strength. The hybrid composites fractured layer reveals damaged matrix and particle interfaces indicating that the shear stress at the interface has not exceeded the fractured strength of particles. The reinforcing particles restrict the motion of the dislocations and control the plastic deformation. Shiny granular interfaces along with dull luster matrix in the composite layer show a quasi-intergranular cleavage fracture of the composite layer. The path of the crack in the region of the particles, debonded/loose particles, dimples, and cleavage facets are observed in the fractography of hybrid composites and there is no indication establish of fractured particles in the composite layers (Prabhu et al., 2014).

The EDAX analysis of fractured surface of developed materials is performed to reveals the compositional details inside the materials as revealed in Fig. 4.10. Figure 4.10 (a) exhibits the EDAX spectrum of fractured surface of CC which displays the intensity peak of oxygen and copper only with their weight and atomic percentage, the reason of oxygen peak present has been discussed earlier. Although, the weight and atomic percentage of oxygen is lower as compared with weight and atomic percentage of oxygen in EDAX spectrum of CC

without fracture as shown in Fig. 4.4 (a). It is observed that the oxidation is higher on outer zone compared with inner zone of CC. The EDAX spectrum of fractured surface of HC-1 as shown in Fig. 4.10 (b) and it is observed that there is no Zr intensity peak, however, rest elemental intensity peaks are observed with their weight and atomic percentage. The absence of Zr intensity peak may be attributed to the pull out of the zirconia from the selected area for EDAX characterization during tensile test. The similar case is observed in the EDAX spectrum of HC-2 where, the Al intensity peak is not found, however the rest of elemental intensity peaks are observed. The EDAX spectrum of HC-3 and HC-4 reveals the intensity peak of all the reinforcing elements with their weight and atomic percentage without any additional elemental intensity peaks as revealed in Figs. 4.10 (d) and (e) respectively. This is also suggested that all the reinforcing elements are found and homogeneously distributed in the copper matrix.

4.5.2. Tertiary reinforced copper-based hybrid composites

Figures 4.11 (a) to (e) show the EDAX spectrum of the CC, HC-5, HC-6, HC-7, and HC-8, respectively. EDAX spectrum reveals the presence of the reinforcing elements of WC, B_4C, BN, and Cr in the hybrid composites shown by their respective peak intensity, weight, and atomic percentage. All elements can be detected in principle, though not all instruments are equipped for elements with low atomic number (Agarwal, 1991; Goldstein, 2003). Therefore, the intensity peak of boron element is absent in the entire EDAX spectrum of the hybrid composites. The intensity peak of the oxygen is observed in the entire EDAX spectrum as shown in Figs. 4.1 (a) to (e). It may be attributed to the presence of residual

oxygen in furnace which resulting oxidation of copper. EDAX analysis confirms that the developed materials posses all the reinforcing materials.

Figures 4.12 (a) to (e) show the typical microstructure of the CC, HC-5, HC-6, HC-7, and HC-8, at 100× magnification. The changes in the microstructure of hybrid composites can be easily observed compared with CC microstructures, which means the reinforcement of the ceramic particles have played a significant role in the copper matrix. It is also observed that the grain refinement takes place in microstructure of HC-5, HC-6, and HC-7 as shown in Fig. 4.12 (b) to (d) respectively, which plays a very important role in the improvement of strength of the HC-5, HC-6, and HC-7. It is due to the reinforcing particles, which restrain the degree of freedom of grain boundaries and further stop the grain growth so that it is limiting the average grain size of the microstructures (Rajkovic et al., 2014). The microstructure of the CC shows twins and these twins (Σ3) grain boundaries contain various facets with different crystallography that is clearly depicted in Fig. 4.12 (a) and Fig 4.13. It may be possible in other copper-based hybrid materials also. However, faceting is a well-recognized occurrence for both interfaces and surfaces, particularly, grain boundaries. Faceting can be considered as a phase evolution when the grain boundaries or original surface breaks into flat segments whose energy is lower than the grain boundary or original surface. Grain boundary faceting proceeds merely near to the boundary so-called coincidence misorientation (Straumal et al., 2001). The Σ9 grain boundary is unbalanced against the reaction of dissociation: $\Sigma 9 \rightarrow \Sigma 3 + \Sigma 3$. Therefore, elongated twins with well-developed Σ3 grain boundaries appear during the growth of crystal, instead of planes or facets. Faceting is a temperature- and composition-dependent phenomenon of the copper alloys where we anticipate that at higher temperature merely the facets with highest density of coincidence

sites become visible, and with declining temperature, various existing facets will slowly increase, including the facets with less dense packed coincidence sites and shallower energetic minima (Straumal et al., 2006).

The microstructure of CC and sections of Σ3 CSL at right angles to the {110} gradient axis with position of different facets and micrograph of intersections of $(100)_{CSL}$ with other facets are shown in Fig 4.13. Thus, micrographs in Figs. 4.12 and 4.13 witnesses that the materials studied, indeed have different amount of twins as well as differences in their facets. In turn, the character of grain boundaries present in the samples could strongly influence their properties.

Figures 4.14 (a) to (d) show the HR-SEM microstructure of the developed hybrid composites i.e. HC-5, HC-6, HC-7, and HC-8 respectively. It is observed from Fig. 4.14 that the ceramic-reinforced particles are visible and fairly well distributed in the copper matrix. This is an indication that the stir-casting process for the development of copper hybrid composites is reliable. HR-SEM micrograph of HC-5 observed quite agglomeration of the reinforcing materials in the copper matrix as depicted in Fig. 4.14 (a) and also observed the porosity. However, the presence of interface reaction is not observed in the HR-SEM micrograph of the hybrid composites as shown in Fig. 4.14.

Figures 4.15 (a) to (e) show the HR-SEM morphology of CC, HC-5, HC-6, HC-7 and HC-8 with selected area for corresponding color dot mapping, shown in Figs. 4.15 (a') to (e') and respective EDAX spectrum as shown in Figs. 4.15 (a") to (e"). This investigation is accomplished to make sure that the developed hybrid composites contain the reinforcing particles. Figure 4.15 (a') shows the color dot mapping of the selected area in HR-SEM micrograph of CC that does not display the color dots apart from the oxygen and copper. The

presence of oxygen and copper in terms of weight and atomic percentage is reported in EDAX spectrum as shown in Fig. 4.15 (a''). The existence of oxygen is due to the possible oxidation of copper with the residual oxygen at high temperature during casting. However, HR-SEM morphology of HC-5, HC-6, HC-7 and HC-8 exhibit the distribution of all reinforcing materials and their presence that is assured by their respective color dot mapping of the selected area. Color dot mapping of respective hybrid composites shows the significant presence of different reinforcing elements including its matrix, which are designated with different color coding. The color coding of each elements with their percentage are highlighted on the top right corner of the respective dot mappings, as shown in Fig. 4.15 (b') to (e'). However, corresponding EDAX spectrum of the materials reveals the significant presence of the reinforcing elements with their weight and atomic percentage, as shown in Figs. 4.15 (b'') to (e''). From the EDAX spectrum, it is observed that the weight and atomic percentage of B and C elements increases as the reinforcing percentage of B_4C in copper increases from 0 to 2 wt%. This investigation concludes that the developed hybrid composites contain the reinforcing particles.

Figure 4.16 (a) shows the HR-XRD pattern of CC, HC-5, HC-6, HC-7, and HC-8. The results have verified with JCPDS data file. It has been observed that copper-based hybrid composites contain all the original peaks of copper, and no additional peak found in the diffraction pattern. However, HC-5 and HC-6 observed few copper oxide peaks along with copper peaks. The absence of the additional peak of reinforcing particles is attributed to low weight percentage (less than 5 wt%) of reinforcing materials into the copper matrix (Samal et al., 2013). However, the sharp peak of HR-XRD pattern indicates the better crystallinity of the grown crystal. The HR-XRD pattern of hybrid composites exhibits slight change in peak

intensity as compared with CC. It attributes to the improved crystallographic perfection of hybrid composites at their concentration along the plane observed by HR-XRD. It may be attributed due to presence of reinforcing elements into the lattice of pure copper materials (Hasmuddin et al., 2014; Ananthi, 2011; Xu et al., 2006). The peak broadening was observed in the enlarged view of diffraction plane (222) at diffraction angle of $2\theta = 95.097^{o}$ as shown in Fig. 4.16 (b). It is attributed to the effect of ceramic-reinforcement in the copper matrix. It was also observed that as the percentage of B_4C increases from x = 0 to x = 1.5 wt%, the peak shifted to the left and become broader as compared with CC peak. The broadening of the Bragg peak is attributed to the decrease in crystallite size.

To understand the Bragg peak broadening in the HR-XRD pattern of the copper hybrid composites, the full width at half maxima (FWHM or β) was calculated for every peak at each diffraction angle for all developed materials. Table-4.3 shows the details of peak positions, diffraction planes, and their respective FWHM. Increase in FWHM indicates the decrease in crystallite size.

Figure 4.17 shows the effect of wt. % of B_4C on FWHM of the HR-XRD peaks. It was observed that as the wt% of B_4C increases up to 1.0 wt%, the FWHM increases up to 0.2478^{o}, but it comes down to 0.1637^{o} when the wt% of B_4C goes to 1.5 wt%. It means that there is decrease in the broadening of peak but this broadening is still more in comparison to the first-two compositions' broadening. This broadening of peak is the consequence of the reduction in the crystallite size and such reduction in crystallite size is possible due to the anomalous broadening effect.

Williamson–Hall (W–H) investigation (Williamson and Hall, 1953) of the FWHM (β) of various Bragg peaks, as shown in Fig. 4.18, is carried out to know the source of the

anomalous broadening of HR-XRD Bragg peaks due to addition of different wt% of B_4C with exclusion of $K\alpha_2$ involvement and instrumental broadening effects. Figure 4.18 shows the W-H plot, a relation between $\beta \cos \theta/\lambda$ and $\sin \theta/\lambda$, where θ is the Bragg's angle. For CC, the plot was likely to be a straight line parallel to the $\sin \theta$ axis, but it shows some slope due to presence of a small internal strain. It was also observed that the gradient of the linear fit always nearly same for 0 wt% of B_4C, but increases significantly on increasing the B_4C from 0.0 to 1.0 wt%. The crystallite size and strain calculated from the W–H plot is enumerated in Table 4.4. The W–H study reveal that the crystallite size decreases by about 48.5 % on increasing the B_4C from 0.0 to 1.0 wt%, whereas strain increases by 96.40 %. This inferred that the anomalous broadening of the peak as shown in Fig. 4.16 (b) is not merely due to crystallite size, but also owing to considerable increase in strain. From Fig. 4.18, it was observed that all the points do not lie on straight line for all the wt% of B_4C; it inferred that the strain is anisotropic for all compositions (Rath et al., 2009).

Table 4.5 shows the variation of experimental, theoretical, relative density, porosity and electrical conductivity of CC, HC-5, HC-6, HC-7, and HC-8. From the Table 4.5, it is observed that the experimental density of the copper hybrid composites decreases with the increasing wt% of B_4C reinforcement with constant wt% of WC and BN into the copper matrix. It is attributed to the addition of low density ($g.cm^{-3}$), irregular shape, and size of B_4C (2.52 $g.cm^{-3}$) and BN (2.1 $g.cm^{-3}$) reinforcements (Prabhu et al., 2014). As shown in Table 4.5, there is some enhancement in experimental density of HC-7 observed as compared with other hybrid composites but not more than CC. This may be attributed to the lowering in porosity due to proper orientation and well-occupied space by reinforcing materials into the copper matrix. The porosity of the materials is reported in the Table 4.5 which shows the

lowest value for HC-7. However, experimental density of hybrid composites i.e. HC-5, HC-6, and HC-8 is decreasing with increasing content of reinforcement. It is due to the increase of the porosity in the hybrid composites, increase in porosity is attributed to the addition of the irregular shape and different size of reinforcing particles into the matrix with their different crystal geometry, such as rhombohedral, hexagonal, and bcc. In addition to this, some clustering of reinforcing phases in the matrix may also favor in enhancement of porosity in the materials as observed in Fig. 4.14 (a).

Table 4.5 also shows the electrical conductivity of CC and tertiary hybrid composites. In the current investigation, electrical conductivity is reported in terms of the percentage International Annealed Copper Standards (% IACS). It is observed that the electrical conductivity decreases with increase in wt% of B_4C with constant wt% of WC and BN. The electrical conductivity decreases from 85 (of CC) to 43 % IACS (of HC-5) with the addition of 1.5 wt% WC and 1 wt% BN with zero wt% of B_4C into the copper matrix. Moreover, the 43 % IACS electrical conductivity of HC-5 decreases to 32 % IACS (of HC-6) when wt% of B_4C increases from 0 to 0.5 with the same amount of WC and BN. Further, decrease in electrical conductivity from 32 (of HC-6) to 25 % IACS (of HC-7) and from 25 (of HC-7) to 19 % IACS (of HC-8) are observed when the wt.% of B_4C increases from 0.5 to 1.0 and 1.0 to 1.5, respectively, with similar amount of WC and BN. Loss of 49.41, 62.35, 70.58, and 77.64 % IACS is observed in HC-5, HC-6, HC-7, and HC-8, respectively, with respect to CC. Here, these hybrid composites are showing a lower conductivity compared with CC (ranging from 78 to 92 % IACS) (Shen et al., 2016). Lowering in the electrical conductivity of hybrid composites are due to the reinforcement of the mostly non-conducting ceramic materials, such as WC, BN, and B_4C into the copper matrix (Nadkarni et al., 1984). In

addition to this, decrease in electrical conductivity of hybrid composites may also be attributed to the presence of porosity as enumerated in Fig. 4.14. Since, the presence of a conductive network is essential for achieving high electrical conductivity. Where, a particle-particle interaction develops the network of conductive path within the developed hybrid composites. So, on the addition of higher amount of ceramic-reinforcement into copper matrix, porosity is introduced (as shown in Fig. 4.14) in the hybrid composites, which disturb the network continuity in the conductivity path (Grant et al., 1984; Ayyappadas et al., 2017).

Figure 4.19 (a) displays the behavior of the Brinell hardness of CC, HC-5, HC-6, HC-7, and HC-8. It is observed that there is a significant increase in the Brinell hardness of hybrid composites with increase in B_4C content from 0.0 to 1.0 wt%. The presence of hard B_4C with other reinforcements increases the Brinell hardness of hybrid composites with increasing their content (Wang et al., 2017). Similar trend was also reported for reinforcement of SiC, B_4C, and AlB_2 particles to enhance the hardness of the composites (Yuan, 2016; Kumar, 2017). Such enhancement in hardness may be attributed to the variation in the plastic deformation of composites due to the reinforcement of hard ceramic particles in softer matrix (Zhang et al., 2014). The hardness of the developed hybrid composites may also be influenced by other reasons, such as their low crystallite size, which was calculated by W-H plot as discussed above, by grain refinement that is observed in microstructures (Zhang et al., 2014), and elastic modulus and thermal mismatch between reinforcing particles and matrix (Ramesh et al., 2009). In addition to this, the improvement in hardness of hybrid composites may be increases due to the involvement of Hall-Petch and Orowan strengthening mechanisms in addition to the interface between the matrix and reinforcements (Sharma et al., 2015).

From the Fig. 4.19 (b), it is clear that the compressive strength of the hybrid composites is higher than CC. The percentage enhancement in the compressive strength is 24.65, 32.87, 52.05, and 53.42% of HC-5, HC-6, HC-7, and HC-8, respectively, with respect to CC. It is attributed to the presence and proper dispersion of the harder ceramics phase into the matrix (Chawla and Shen, 2001). Such improvement in compressive strength of hybrid composites is due to the load transfer effect, i.e. under an applied load the load is transferred from the softer matrix via interface of the ceramic and copper matrix to the normally higher stiffness ceramic-reinforcements. In this way, strengthening takes place by the reinforcement of ceramic carrying almost all the applied load. Although the reinforcing particles have a low aspect ratio, it is still significant in providing compressive strength to the developed composite materials (Chawla and shen, 2001; Zhang et al., 2004). The compressive strength of the hybrid composites may also be improve due to the variation in coefficient of thermal expansion of reinforcing particles and matrix, which increase the density of dislocation at the interface of matrix and reinforcement due to which the compressive strength is improved (Nguyen et al., 2008). In addition to this, the refined grain also plays a vital role in the enhancement of strength (Hassan et al., 2003) including Orowan strengthening (Nguyen et al., 2009). Therefore, these combined strengthening mechanisms are responsible for improved compressive strength of the hybrid composite materials.

An improvement in ultimate tensile strength (UTS) is achieved with the increase in B_4C content from 0 to 1.0 wt% as shown in Fig. 4.19 (c). An improvement of 16.2, 27.6, 50.4, and 39.0% in UTS is observed for HC-5, HC-6, HC-7, and HC-8, respectively. It may be due to the combined effect of improved hardness of the hybrid composites (Jha et al., 2016) and increased wettability of copper matrix by addition of Cr. Wettability is an

influencing factor to ensure good bonding between the matrix and reinforcements and; good bonding is always required for the improvement of UTS of materials (Wang et al., 2017). In addition, the lowering in crystallite size and grain refinement of the developed hybrid materials may also play a vital role in the improvement of UTS of the materials. HC-7 displays the highest UTS among all, as shown in Fig. 4.19 (c). It is also noticed that HC-8 has higher UTS than other developed hybrid composite materials and matrix but lower than HC-7, because of its lower density and hardness compared with HC-7. UTS of composites may also be enhanced by the incorporation of ceramic particles in copper matrix that increase the work hardening in the materials. The work hardening in the hybrid composites is due to the geometric constraints forced by the existence of the ceramic reinforcement. When the matrix is considerably strain hardened, the matrix is to be found under huge constraints with an incapability of the strain reduction. (Bhagyashekhar et al., 1997).

Figures 4.20 (a) to (e) and 4.21 (a) to (e) exhibit the SEM morphology of the fractured surface of CC, HC-5, HC-6, HC-7, and HC-8 at 70 and 2000× magnification respectively. Figures 4.20 (a) to (e) reveal the typical fractures involve with tensile test. Ductile fracture has two types of geometry, such as, cup and cone, whereas brittle fracture shows the flat surface gesture. It is observed that the CC has a cup type of failure, which clearly indicates its ductile nature as shown in Fig. 4.20 (a). However, the fracture face of hybrid composites shows approximately flat surfaces, which confirms that the developed hybrid composites have brittle fracture nature. It is due to the improvement in the hardness of the developed hybrid composites attributed to the reinforcement of hard ceramic particles into the matrix. The fracture surface of the HC-7 at 70× magnification shows the maximum flatness, which confirm that it is the most brittle and hardened among all, as shown in Fig.

4.20 (d). Morphology of the CC at 2000× magnification reveals larger size of dimples indicates the ductile fracture behavior. Such larger dimples are the consequence of the coalescence of the localized micro voids (Wang et al., 2017; Szaraz et al., 2007) as shown in Fig. 4.21 (a'). The micrograph of the fractured surface of HC-5, HC-6, HC-7, and HC-8 at 2000× magnification shows smaller dimples compared with CC, which indicate the brittle nature of fracture as shown in Figs. 4.21 (b') to (e'). The fractography of the highest strengthened HC-7 shows a unique geometry, such as strong networking-like spider nets, as shown in Fig. 4.21 (d'), with almost zero micro voids. Such new geometry of fractography strongly recommends consideration of the high strength and brittle nature of materials.

Figures 4.22 (a) to (e) show the EDAX spectrum of the fracture surface of CC, HC-5, HC-6, HC-7 and HC-8 respectively. Fracture faces of the materials are investigated through EDAX to observe the significant presence of reinforcing particles in the materials. In the EDAX spectrum of CC, additional intensity peaks are not found other than oxygen and copper intensity peak. The detail explanation regarding presence of oxygen in the spectrum has been given above, due to the oxidation of copper at high temperature. The EDAX spectrum of the entire hybrid composites does not show the intensity peak of boron due to its low atomic weight that is quite difficult to detect. Though, intensity peaks of almost all the reinforcing elements are seen in the entire EDAX spectrum of hybrid composites. The EDAX spectrum of the HC-6 and HC-7 unable to show the intensity peak of chromium, while the intensity peaks of other elements are observed as shown in Figs. 4.22 (c) and (d). It may be attributed to the insignificance presence of chromium element in the selected area for the investigation.

In comparative study of the binary and tertiary hybrid composites, it is found that almost all the properties of the tertiary hybrid composites are better as compared with the binary hybrid composites. It may be attribute to the more homogeneous dispersion of the reinforcing phases in the matrix and significantly higher interfacial bonding between the matrix and reinforcements. In addition to this, the porosity developed in the tertiary hybrid composites is lower than that of binary hybrid composites that is shown in Table 4.6 which leads to the good strength of the materials. However, the tertiary hybrid composites show the poor electrical conductivity as compared to binary reinforced hybrid composites that is because of addition of lower conducting reinforcements in the matrix as compared to binary reinforcements.